Engineering Analysis with Boundary Elements 159 (2024) 17–35

Contents lists available at ScienceDirect

Engineering Analysis with Boundary Elements

journal homepage: www.elsevier.com/locate/enganabound

Improved hole and tube elements in BEM for elasticity problems

Yong-Tong Zheng [a,b,*], Yijun Liu [a], Xiao-Wei Gao [b,c], Yang Yang [a], Hai-Feng Peng [b]

[a] Department of Mechanics and Aerospace Engineering, Southern University of Science and Technology, Shenzhen 518055, China
[b] School of Aeronautics and Astronautics, Dalian University of Technology, Dalian 116024, China
[c] State Key Laboratory of Structural Analysis for Industrial Equipment, Dalian University of Technology, Dalian 116024, China

ARTICLE INFO

Keywords:
Boundary element method
Iso-parametric closure elements
Hole elements
Stress concentration

ABSTRACT

Structures with holes are prevalent in engineering applications. Analyzing the stress concentration effects caused by holes using the finite element method (FEM) or the boundary element method (BEM) is challenging and time-consuming. Typically, a large number of elements are necessary in the vicinity of holes to achieve accurate results. In this paper, a series of improved hole elements and tube elements are constructed for simulating the holes and cylinders, respectively. Two construction methods for hole elements, based on Lagrange and trigonometric interpolations, respectively, are introduced. The general formulas for evaluating singular integrals over the proposed elements are derived. Additionally, the adaptive element sub-division technique is applied to address the nearly singular integrals over these elements and account for the interactions of multiple holes. Five numerical examples are studied to demonstrate the accuracy and efficiency of the proposed elements. The results demonstrate that employing hole and tube elements can reduce the number of nodes while maintaining stress accuracy, in comparison to using several quadratic elements.

1. Introduction

Holes are frequently encountered in structural design, whether they are for bolts, film-cooling on engine blades, and so on. Some holes may be intended for reducing weight, while some holes may serve to accommodate the passage of other components. Regardless of their design purpose, holes will alter the stress distribution in the vicinity, leading to stress concentration.

In general, engineers employ numerical methods to obtain the stress distribution over the structures, such as the finite element method [1–3] (FEM) and boundary element method [4–6] (BEM). Achieving accurate analysis of stress concentration around holes with the FEM requires a dense distribution of nodes and quadratic elements within the computational domain, particularly when the hole size is significantly smaller than the overall structure. Consequently, employing FEM complicates mesh generation and increases computational time. In the case of the BEM, only the boundaries of the computational domain are discretized, eliminating the need for intricate mesh generation within the computational domain. Nevertheless, refined discretization of the holes is still essential to achieve accurate stress distributions in their vicinity. A conventional and viable method involves employing numerous constant elements, linear elements, or quadratic elements to approximate circular or elliptical geometries and interpolate variables over them. This implies that a substantial number of nodes are still required around the holes, potentially leading to high computational costs.

Therefore, some researchers have constructed boundary elements resembling holes and developed associated techniques to address circular geometries, such as holes, cylinders, and spheres, based on BEM. Henry and Banerjee et al. constructed a 3-node trigonometric hole element to simulate displacements and temperatures around the holes. They streamlined the boundary integral formulas by considering the geometrical characteristic, resulting in reduced computational costs [7–10]. Buroni et al. expanded the hole elements to 4, 5 and 6 nodes to simulate the cylindrical voids within the domain. They also devised techniques for evaluating weakly and strongly singular integral over these elements [11,12]. However, Buroni et al. did not consider the impact of closely spaced holes, neglecting the consideration of nearly singular integrals. Zhang's team created a tubular element based on 3-node hole element to simulate the open-ended tubular holes. They integrated these elements in boundary face method to analyze the distributions of temperature [13], stress [14] and acoustic pressure [15] over the relevant structures. Feng et al. designed specialized boundary elements to discretize a spherical surfaces with high geometrical accuracy when analyzing the acoustic properties of spheres [16].

* Corresponding author.
E-mail address: zhengyt@sustech.edu.cn (Y.-T. Zheng).

https://doi.org/10.1016/j.enganabound.2023.11.021
Received 10 July 2023; Received in revised form 28 October 2023; Accepted 20 November 2023
Available online 25 November 2023

Recently, a series of isoparametric closure elements were proposed by Gao et al. [17–19], containing hole elements, tube elements, ring elements, disk elements, and sphere elements as depicted in Fig. 1. Different from the hole elements mentioned above, their hole elements are derived by the Lagrange polynomial interpolation formulation and closure conditions at two ends of an arc. The tube and ring elements can be created by multiplying the shape functions of the corresponding nodes in the hole elements and line elements. The disk and sphere elements are formed by summing the shape functions of the associated nodes on the ring and tube elements, respectively. The evolutionary relationships between these elements are illustrated in Fig. 2. It is evident that the hole element serves as the foundation for these elements, and the accuracy of the hole element impacts its derived elements.

However, the accuracy of the Lagrange hole elements is not satisfactory in geometrical discretization when the node count is less than 8. Therefore, Ma et al. constructed an 8-node hole element with improved smoothness by incorporating two auxiliary nodes into the expanded Lagrange polynomial interpolation functions [20,21]. This element performs better in the mechanics problems than those created by merely closing two ends of an arc.

In summary, the construction of the hole elements serves as the foundation for the construction of the isoparametric closure elements. Hence, it is necessary to investigate the accuracy of hole elements with varying number of nodes and different interpolation methods. The authors believe that the previously proposed hole elements may lack the necessary accuracy in simulating stress concentration effect of closely spaced holes. Therefore, in this paper, the authors will follow the improvement idea from Ma to enhance the accuracy of Lagrange hole elements by introducing more auxiliary nodes. Meanwhile, the trigonometric hole elements are expanded to include 8-node, 12-node, and 16-node versions. Then, based on the hole element, the tube elements are constructed to simulate the cylindrical holes in three-dimensional models. An adaptive element sub-division technique will be applied to evaluate the nearly singular integrals over the proposed elements. Finally, the authors will compare the performance of two interpolation hole elements in simulating stress concentration effect on the holes. They will also verify the necessity of employing trigonometric hole elements with more nodes and the high accuracy of the tube elements based on trigonometric interpolation.

The rest of the paper is organized as follows. First, some basic BEM formulas are presented. Second, the construction concepts for the Lagrange, trigonometric hole elements and tube elements are discussed. Third, the methods for evaluating singular and nearly singular integrals over the hole and tube elements are introduced. Then, five examples are given to compare the accuracy of the proposed elements when simulating the plate with single small circular hole, single elliptic hole, double circular holes, randomly positioned multi-holes and the cubic structure with cylindrical holes. Finally, some conclusions are drawn to summarize the paper.

2. Brief introduction of BEM for elasticity problems

For elasticity, the boundary integral equation (BIE) can be expressed as follows [4–6]:

$$cu_i(P) = \int_\Gamma u_{ij}^*(P,Q)t_j(Q)d\Gamma(Q) - \int_\Gamma t_{ij}^*(P,Q)u_j(Q)d\Gamma(Q) \tag{1}$$

where u_j and t_j are the displacements and tractions on the boundary Γ at the j-th direction; P and Q represent the source point and the field point, respectively; u_{ij}^* and t_{ij}^* are the Kelvin's fundamental solutions, which can be written as:

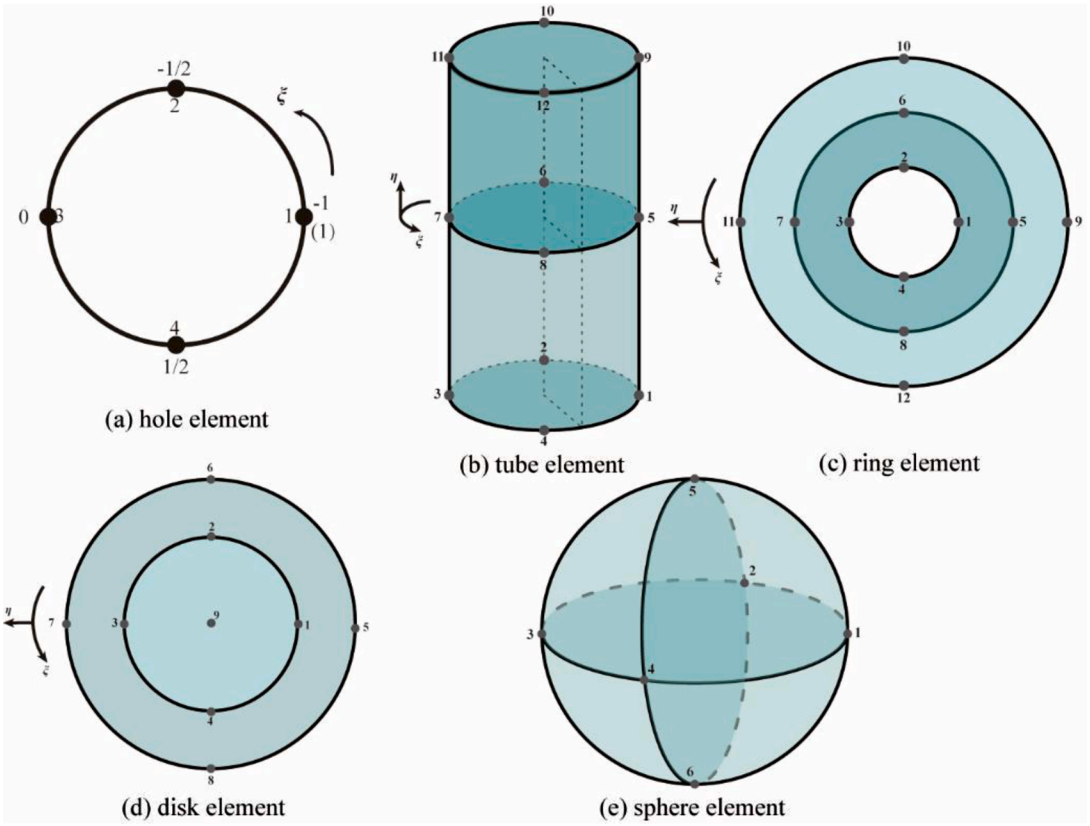

Fig. 1. The isoparametric closure elements.

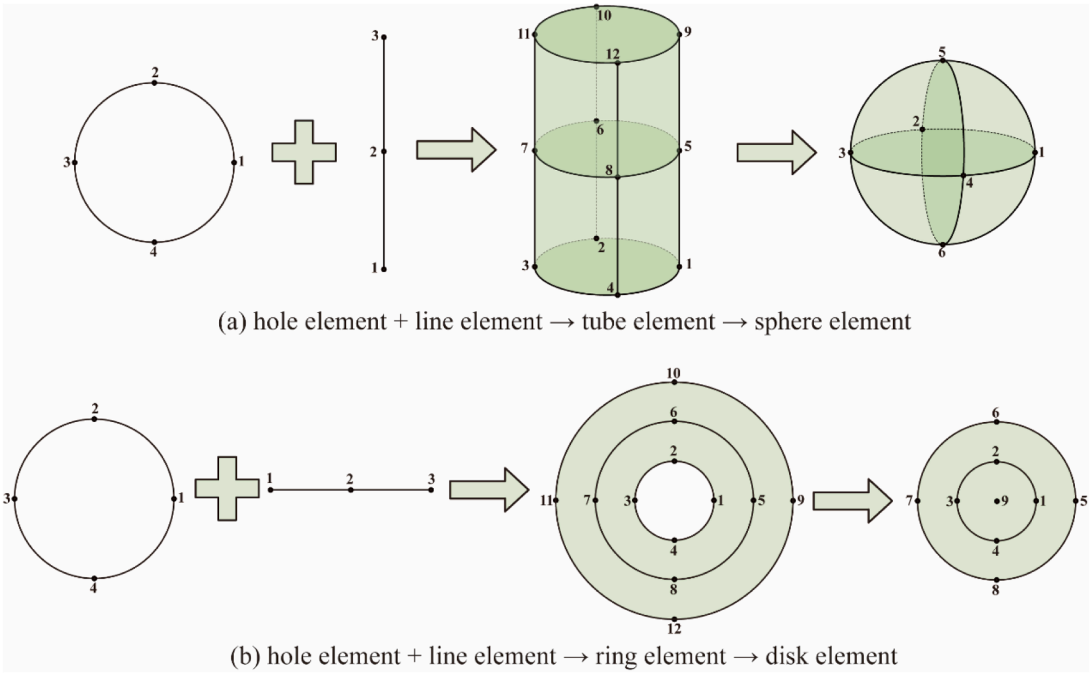

Fig. 2. The evolutionary relationships between isoparametric closure elements.

$$u_{ij}^{*}=\begin{cases}\dfrac{1}{8\pi(1-\nu)\mu}\left[(3-4\nu)\delta_{ij}\ln\left(\dfrac{1}{r}\right)+\dfrac{\partial r}{\partial x_i}\dfrac{\partial r}{\partial x_j}\right]\text{for2D}\\ \dfrac{1}{16\pi(1-\nu)\mu r}\left[(3-4\nu)\delta_{ij}+\dfrac{\partial r}{\partial x_i}\dfrac{\partial r}{\partial x_j}\right]\text{for3D}\end{cases}\tag{2}$$

$$t_{ij}^{*}=-\frac{1}{4\pi\alpha(1-\nu)r^{\alpha}}\left\{\frac{\partial r}{\partial n}\left[(1-2\nu)\delta_{ij}+\beta\frac{\partial r}{\partial x_i}\frac{\partial r}{\partial x_j}\right]+(1-2\nu)\left(n_i\frac{\partial r}{\partial x_j}-n_j\frac{\partial r}{\partial x_i}\right)\right\}\tag{3}$$

in which μ is the shear modulus; ν is the Poisson ratio; β is the dimension of the problems and $\alpha=\beta-1$; the subscripts i and j obey Einstein summation convention (the same hereinafter).

The BIE for calculating interior stresses can be expressed as follows:

$$\sigma_{ij}(P)=\int_{\Gamma}U_{ijk}^{*}(P,Q)t_k(Q)\mathrm{d}\Gamma(Q)-\int_{\Gamma}T_{ijk}^{*}(P,Q)u_k(Q)\mathrm{d}\Gamma(Q)\tag{4}$$

where U_{ijk}^{*} and T_{ijk}^{*} can be calculated by the following two formulas:

$$U_{ijk}^{*}=\frac{1}{4\pi\alpha(1-\nu)r^{\alpha}}\left[(1-2\nu)\left(\delta_{ik}\frac{\partial r}{\partial x_j}+\delta_{jk}\frac{\partial r}{\partial x_i}-\delta_{ij}\frac{\partial r}{\partial x_k}\right)+\beta\frac{\partial r}{\partial x_i}\frac{\partial r}{\partial x_j}\frac{\partial r}{\partial x_k}\right]\tag{5}$$

$$\begin{aligned}T_{ijk}^{*}=&\frac{\mu}{2\pi\alpha(1-\nu)r^{\beta}}\left\{\beta\frac{\partial r}{\partial n}\left[(1-2\nu)\delta_{ij}\frac{\partial r}{\partial x_k}+\nu\left(\delta_{ik}\frac{\partial r}{\partial x_j}+\delta_{jk}\frac{\partial r}{\partial x_i}\right)-\gamma\frac{\partial r}{\partial x_i}\frac{\partial r}{\partial x_j}\frac{\partial r}{\partial x_k}\right]\right.\\&\left.+\beta\nu\left(n_i\frac{\partial r}{\partial x_j}\frac{\partial r}{\partial x_k}+n_j\frac{\partial r}{\partial x_i}\frac{\partial r}{\partial x_k}\right)+(1-2\nu)\left(\beta n_k\frac{\partial r}{\partial x_i}\frac{\partial r}{\partial x_j}+n_j\delta_{ik}+n_i\delta_{jk}\right)+(1-4\nu)n_k\delta_{ij}\right\}\end{aligned}\tag{6}$$

where $\gamma=\beta+2$.

To evaluate the boundary integrals in Eqs. (1) and (3), boundary Γ could be discretized into boundary elements, where the displacements, surface tractions and even geometric coordinates are interpolated by the same shape functions, i.e.

$$u_i(\xi)=N_{\alpha}(\xi)u_i^{\alpha}\tag{7}$$

$$t_i(\xi)=N_{\alpha}(\xi)t_i^{\alpha}\tag{8}$$

$$x_i(\xi)=N_{\alpha}(\xi)x_i^{\alpha}\tag{9}$$

in which N_α is the shape functions; α represents the α-th node and the repeated scripts α also obeys Einstein summation convention; ξ is the intrinsic coordinate on the element, range from -1 to 1.

After discretizing the boundaries of the computational domain, if regarding each boundary node as the source point, one node corresponds two or three algebraic equations. By assembling these equations together, a system of linear algebraic equations can be derived as follows:

$$[H]\{u\}=[G]\{t\}\tag{10}$$

in which $\{u\}$ and $\{t\}$ are the displacement and surface traction vector containing the displacements and surface tractions of all the boundary nodes, respectively; $[H]$ and $[G]$ are the coefficient matrix. By rearranging the equation, with unknowns on the left-hand side and known terms on the right, and then solving the resulting system, the displacements and surface tractions at each node will be obtained. Next, by substituting these values into the discretized stress BIEs, the stress at source point P can be obtained. Specially, if source point P is on the boundary, the hyper-singular and strong-singular integrals should be evaluated according to the Eqs.(3)-(5). To avoid that, in this paper, the traction recovery method [5] is employed to calculate the stresses on the boundaries.

3. Construction of the improved hole and tube elements

In this section, Lagrange and trigonometric hole elements, as well as tube elements are introduced, including their intrinsic coordinate system, node distributions, shape functions and so on. Additionally, the node distributions of the hole elements on the ellipse will be discussed because of the asymmetry of ellipse.

3.1. "Repeated winding" Lagrange hole elements

The Lagrange hole elements are proposed by Gao et al. [17], with shape functions derived from the Lagrange line elements by adding one extra node. This constructing method is called "end to end". The α-th node's shape function of the N-node line element can be expressed as

$$N_\alpha(\xi)=\prod_{i=1,i\neq\alpha}^{N}\frac{\xi-\xi_i}{\xi_\alpha-\xi_i}\,1\le\alpha\le N \tag{11}$$

Consequently, the α-th node's shape function of (N-1)-node hole element can be expressed as

$$N_\alpha(\xi)=\begin{cases}\prod_{i=2}^{N}\frac{\xi-\xi_i}{\xi_1-\xi_i}+\prod_{i=1}^{N-1}\frac{\xi-\xi_i}{\xi_N-\xi_i}\,\alpha=1\\ \prod_{i=1,i\neq\alpha}^{N}\frac{\xi-\xi_i}{\xi_\alpha-\xi_i}\,1<\alpha\le N-1\end{cases} \tag{12}$$

For example, adding up the shape functions of node 1 and node 4 in a 4-node line element, the shape functions of 3-node hole element are obtained, as is shown in the Eq.(13) and Fig. 3.

$$\begin{cases}N_1=-\frac{1}{16}(1-\xi)(1-9\xi^2)\\ N_2=\frac{9}{16}(1-\xi^2)(1-3\xi)\\ N_3=\frac{9}{16}(1-\xi^2)(1+3\xi)\\ N_4=-\frac{1}{16}(1+\xi)(1-9\xi^2)\end{cases}\Rightarrow\begin{cases}N_1'=N_1+N_4=-\frac{1}{8}(1-9\xi^2)\\ N_2'=N_2=\frac{9}{16}(1-\xi^2)(1-3\xi)\\ N_3'=N_3=\frac{9}{16}(1-\xi^2)(1+3\xi)\end{cases} \tag{13}$$

The intrinsic coordinate of first node is −1 or 1, while those of the second and the third are −1/3 and 1/3, respectively. It should be noted that hole elements can only be utilized to simulate the variables (or coordinates) located on the edge of the hole, not within the hole.

However, the elements constructed by "end to end" exhibit low accuracy when the number of nodes is fewer than 8. Fig. 4 shows the results of simulating a unit circle by hole elements with 3 to 8 nodes. The images in Fig. 4 are generated from 1000 points on the elements and the radius error of each point is calculated by (radius-1.0)/1.0 × 100% (all the actual radii are 1). It can be found that 8-node element yields the best performance. The images of 3-node and 4-node elements exhibit significant distortion. The image of 6-node element is not smooth at the first node where two ends of line element are superposed.

To improve the Lagrange hole elements, Ma et al. [20,21] proposed smooth hole elements by adding two supplemental nodes at both sides of the original end node. For example, as depicted in Fig. 5, nodes labeled as 0, 7 and 8 in the 9-node line element on the left, referred to as auxiliary nodes, are positioned to coincide with the nodes 6, 1 and 2, respectively. Then, by summing the shape functions of coincident nodes, the smooth 6-node element is obtained. It should be noted that the intrinsic coordinates of 9-node line element are from −4/3 to 4/3.

Inspired by the idea from Ma et al., the authors believe that more auxiliary nodes can be incorporated to construct higher-order hole elements without increasing the actual number of nodes. This process is akin to winding a string around a circle for several times. Therefore, this construction method can be referred to as "repeated winding." For convenience, in this paper, if the number of nodes in the original line element is denoted as "a", and the number of nodes in the generated hole element is "b", it is called "a-b Lagrange hole element". For example, 9–4 Lagrange hole element represents winding a 9-node line element around a circle twice, as shown in Fig. 6. The shape functions are as follows:

$$\begin{cases}N_1=\frac{1}{45}\left(\xi^2\left(-36+\xi^2\left(13-4\xi^2\right)^2\right)\right)\\ N_2=\frac{1}{315}(-8(-2+\xi)(-1+\xi)\xi(1+\xi)(2+\xi)(-1+2\xi)(3+2\xi)(-5+4\xi))\\ N_3=\frac{1}{315}\left(315+(-2+\xi)\xi^2(2+\xi)\left(449-488\xi^2+144\xi^4\right)\right)\\ N_4=\frac{1}{315}(-8(-2+\xi)(-1+\xi)\xi(1+\xi)(2+\xi)(-3+2\xi)(1+2\xi)(5+4\xi))\end{cases} \tag{14}$$

It should be noted that the shape functions generated by this method still satisfy Kronecker delta properties.

To assess the geometric accuracy of the "repeated winding" hole elements, a unit circle is also simulated by 5–4, 7–4, 9–4, 13–4, 17–4 Lagrange hole elements, whose results are shown in Fig. 7. It is obvious that the more auxiliary nodes are used, the higher geometric accuracy the elements deliver, in terms of 4-node Lagrange hole elements.

3.2. Trigonometric hole elements

Lagrange elements are based on a set of polynomials such as 1, ξ, ξ^2, ξ^3 and so on. Considering the characteristics of the circle or ellipse, intrinsic coordinate ξ can be transformed into another intrinsic coordinate θ, with the relationship denoted as:

$$\theta=\pi(1+\xi)\theta\in[0,2\pi) \tag{15}$$

The nodes are equally distributed around the circumference. The 3-node trigonometric hole element features three nodes with intrinsic coordinates 0, 2π/3, and 4π/3 as depicted in Fig. 8. The bases of trigonometric hole elements are replaced by a series of trigonometric functions, such as 1, cos θ, sin θ, cos$^2\theta$, etc. The coefficients for these bases can be determined by solving the equations derived from Kronecker delta properties of the shape functions. For example, the shape function at the first node in 3-node trigonometric hole elements can be expressed as:

$$N_1(\theta)=a+b\cos\theta+c\sin\theta \tag{16}$$

According to the Kronecker delta property, equations are:

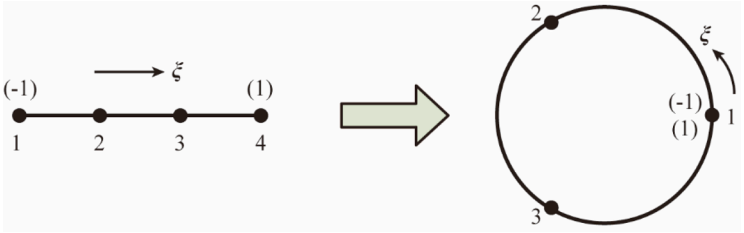

Fig. 3. The 3-node hole element evolved from 4-node Lagrange line element.

Elements	3-node	4-node	6-node	8-node
Images	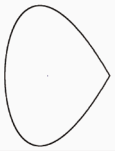		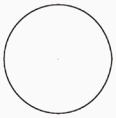	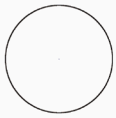
Max radius errors	13.52%	17.92%	0.50%	0.07%

Fig. 4. Results of simulating a unit circle by four kinds of hole elements.

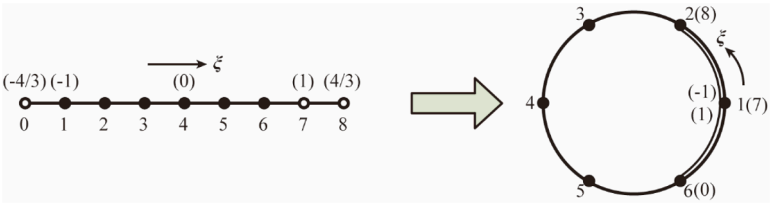

Fig. 5. Construction of the smooth 6-node Lagrange hole element.

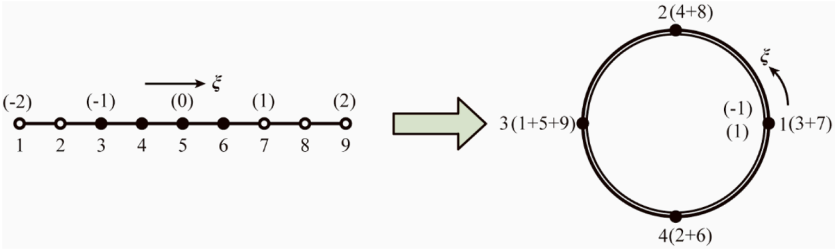

Fig. 6. Construction of 9–4 Lagrange hole element.

Elements	5-4	7-4	9-4	13-4	17-4
Images		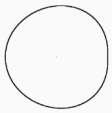			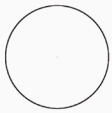
Max radius errors	17.92%	5.5615%	2.1041%	0.3745%	0.07556%

Fig. 7. Results of simulating a unit circle by 5 kinds of 4-node Lagrange hole elements.

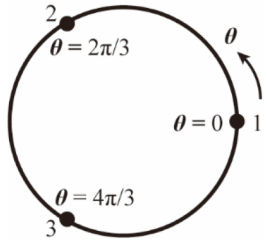

Fig. 8. 3-node trigonometric hole element.

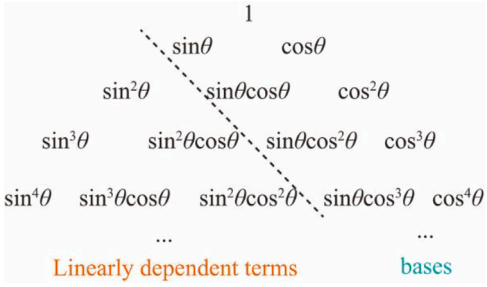

Fig. 9. Pascal triangle for choosing the bases.

$$\begin{cases} N_1(0) = a + b\cos 0 + c\sin 0 = 1 \\ N_1(2\pi/3) = a + b\cos(2\pi/3) + c\sin(2\pi/3) = 0 \\ N_1(4\pi/3) = a + b\cos(4\pi/3) + c\sin(4\pi/3) = 0 \end{cases} \tag{17}$$

By solving *a, b* and *c*, the shape function can be obtained as follows:

$$N_1(\theta) = \frac{1}{3} + \frac{2}{3}\cos\theta \tag{18}$$

Similarly, the other two shape functions can be determined as

follows:

$$\begin{aligned} N_2(\theta) &= \frac{1}{3} - \frac{1}{3}\cos\theta + \frac{\sqrt{3}}{3}\sin\theta \\ N_3(\theta) &= \frac{1}{3} - \frac{1}{3}\cos\theta - \frac{\sqrt{3}}{3}\sin\theta \end{aligned} \tag{19}$$

When constructing the trigonometric hole elements with more nodes, some high order bases should be employed. Fig. 9 illustrates a Pascal triangle with trigonometric function bases. Due to the linear dependence among trigonometric functions, only the terms on the right side of the dotted line are selected as bases, while those on the left are disregarded. For example, the bases of 4-node element consist of 1, $\cos\theta$, $\sin\theta$, $\cos^2\theta$. The bases of 6-node element include 1, $\cos\theta$, $\sin\theta$, $\cos^2\theta$, $\sin\theta\cos\theta$, $\cos^3\theta$. Naturally, this is not the sole method for selecting the bases. One can replace $\cos^2\theta$ by $\sin^2\theta$ as the base for 4-node element, which will result in the same shape functions. The shape functions of 4, 6, 8, 12, and 16-node trigonometric hole elements will be provided in Appendix A, at the last of this paper.

3.3. Node distributions on the ellipse

When simulating a circle, using either the Lagrange or the trigonometric hole elements, the node distributions obey the principle of equally dividing a circle by all the nodes. However, when simulating an ellipse, two options are available. Taking 8-node hole element as the example, the second node can either be positioned at the midpoint of the arc between the first and third nodes, or at the point where the bisector of the angle intersects the arc, as is shown in Fig. 10 (node 4, 6, and 8 encounter a similar situation). For convenience, in this paper, these options are referred to as "arc-middle" and "angle-middle" point, respectively.

So, which one is better for Lagrange and trigonometric hole elements? To give the answers, an ellipse with semi-major axis of 5 and semi-minor axis of 3 is simulated by both node distribution methods and two different types of hole elements, whose results are presented in Fig. 11. Based on these results, it can be inferred that, considering geometric accuracy, angle-middle is superior to the arc-middle for both trigonometric and Lagrange hole elements. Furthermore, the error will not be acceptable if combining arc-middle distributions with Lagrange hole elements.

3.4. Tube elements

Tube elements are derived from the hole elements and line elements. They are 2D elements represented by coordinate ξ for circumferential orientation and coordinate η for longitudinal orientation, and they are used in 3D BEM. The shape functions of the tube elements are derived by the product of the shape functions of hole elements (represented by C_a) and line elements (represented by L_b), which can be expressed as::

$$N_\alpha(\xi,\eta) = C_a(\xi)L_b(\eta) \quad -1 \le \xi,\eta \le 1 \tag{20}$$

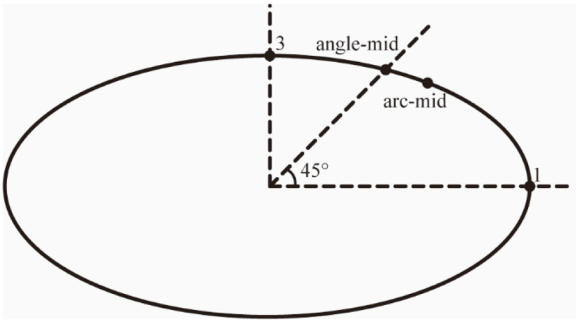

Fig. 10. Two choices of the second nodes: arc-middle and angle-middle.

For example, a 24-node (8 × 3) tube element, as depicted in Fig. 12, is derived from an 8-node hole element and a 3-node quadratic line element. The shape functions for all nodes can be determined by the following formula:

$$N_\alpha(\xi,\eta) = \begin{cases} C_\alpha(\xi)L_1(\eta) & 1 \le \alpha \le 8 \\ C_{\alpha-8}(\xi)L_2(\eta) & 9 \le \alpha \le 16 \\ C_{\alpha-16}(\xi)L_3(\eta) & 17 \le \alpha \le 24 \end{cases} \tag{21}$$

Usually, several tube elements can be used to simulate a straight or curved cylindrical hole, the lateral surface of a cylindrical truncated cone and so on. Generally, the nodal sequence shown in Fig. 12 indicates that the outward normal is oriented away from the center. If the outward normal points towards the center, the sequence along ξ or along η direction should be reversed.

4. Evaluation of singular integrals over the hole element

To achieve accurate results in BEM, it is essential to accurately evaluate the integrals in BIEs. Generally, Gauss-Legendre quadrature formula can be used to calculate regular integrals with a few integration points (in this paper, the number of integration points = 4 × the number of nodes in the element). However, when the source point P is located on the integration element or very close to it, the integral become a singular integral or near-singular integral, respectively. Only considering the portions in the fundamental solution responsible for the singularity, the integrals become:

$$I_w = \begin{cases} \int_{-1}^{1} \ln\left(\frac{1}{r}\right) N_\alpha(\xi) J \mathrm{d}\xi & \text{for 2D} \\ \int_{-1}^{1}\int_{-1}^{1} \frac{1}{r} N_\alpha(\xi,\eta) J \mathrm{d}\xi \mathrm{d}\eta & \text{for 3D} \end{cases} \tag{22}$$

$$I_s = \begin{cases} \int_{-1}^{1} \frac{1}{r} \cdot N_\alpha(\xi) J \mathrm{d}\xi & \text{for 2D} \\ \int_{-1}^{1}\int_{-1}^{1} \frac{1}{r^2} N_\alpha(\xi,\eta) J \mathrm{d}\xi \mathrm{d}\eta & \text{for 3D} \end{cases} \tag{23}$$

$$I_h = \begin{cases} \int_{-1}^{1} \frac{1}{r^2} \cdot N_\alpha(\xi) J \mathrm{d}\xi & \text{for 2D} \\ \int_{-1}^{1}\int_{-1}^{1} \frac{1}{r^3} N_\alpha(\xi,\eta) J \mathrm{d}\xi \mathrm{d}\eta & \text{for 3D} \end{cases} \tag{24}$$

in which I_w, I_s, I_h represent weak-singular, strong-singular, and hyper-singular integrals, respectively. Due to the use of traction recovery method, the evaluation of hyper-singular integrals can be avoided. So, in this section, the weak-singular integrals, strong-singular integrals and nearly weak-, strong-, hyper-singular integrals are mainly concerned.

4.1. Weak-singular integral

Integral in Eq.(21) will become weak-singular when the source point P is located on the integration element.

For hole elements used in 2D problems, r, the distance from the source point P to the field point Q, can be written as:

$$r^2 = (\xi - \xi_P)^2 \left(f_1^2 + f_2^2\right) \tag{25}$$

in which ξ and ξ_P are the intrinsic coordinates of point Q and P, respectively, and

$$f_i = \begin{cases} \frac{N_\alpha(\xi) - N_\alpha(\xi_P)}{\xi - \xi_P} \cdot x_i^\alpha & \xi \ne \xi_P \\ \left.\frac{\partial N_\alpha(\xi)}{\partial \xi}\right|_{\xi=\xi_P} \cdot x_i^\alpha & \xi = \xi_P \end{cases} \tag{26}$$

Elements	trigonometric	trigonometric	17-8 Lagrange	17-8 Lagrange
Node distributions	angle-middle	arc-middle	angle-middle	arc-middle
Images	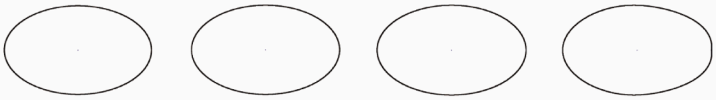			
Max radius errors	1.332×10^{-15}	6.122×10^{-4}	3.387×10^{-8}	4.222×10^{-2}

Fig. 11. Results of simulating an ellipse by two kinds of node distribution methods.

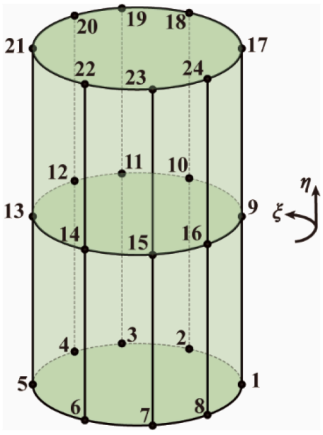

Fig. 12. 24-node tube element.

where repeated α represent summation and subscript i range from 1 to 2. It is obvious that ξ - ξ_P will result in the singular parts of the integrals and the rest terms are regular. Therefore, the integral in Eq (21). becomes:

$$I_w = I_{ws} + I_{wr} = \int_{-1}^{1} \ln\left|\frac{1}{\xi-\xi_P}\right| N_\alpha(\xi) J_\xi \mathrm{d}\xi - \frac{1}{2}\int_{-1}^{1} \ln\left(f_1^2+f_2^2\right) N_\alpha(\xi) J_\xi \mathrm{d}\xi \quad (27)$$

in which I_{ws} and I_{wr} are the singular part and regular part of the weak-singular integral, respectively. Then, the regular part can be calculated by Gauss-Legendre quadrature formula just like other regular integrals, while the singular part can be evaluated by logarithmic quadrature formula, i.e.

$$\int_0^1 \ln\left(\frac{1}{x}\right) f(x)\mathrm{d}x \approx \sum_{i=1}^{n} w_i f(x_i) \quad (28)$$

where the integration points and their weights can be found in the Ref. [22].

In 3D problems involving tube elements, the degenerated element method [5] is employed. First, one can map the tube element to the intrinsic parameter space as shown in Fig. 13, resulting in a square shape. This process is akin to slicing the cylindrical lateral surface along a generatrix ($\xi = \xi_P + 1$ or $\xi = \xi_P$ - 1), which is opposite to the source point. Then, the square can be sub-divided into four triangles by connecting the source point and four corners. Then, one can map each triangle to a 4-node square element where source point corresponds to two nodes, as shown in Fig. 14 (Only for the upper triangle). Describing the process by a formula, the integration takes the form:

$$\int_{-1}^{1}\int_{-1}^{1} \frac{1}{r} N_\alpha J \mathrm{d}\xi\mathrm{d}\eta = \sum_{i=1}^{4}\int_{T_i} \frac{1}{r} N_\alpha J \mathrm{d}\xi\mathrm{d}\eta = \sum_{i=1}^{4}\int_{-1}^{1}\int_{-1}^{1} \frac{1}{r} N_\alpha J\cdot J_{T_i} \mathrm{d}\xi'\mathrm{d}\eta' \quad (29)$$

where Jacobian J_{Ti} at source point P equals zero, which eliminate the singularity caused by $1/r$.

4.2. Strong-singular integral

In this paper, the strong-singular integrals in coefficient matrix [H] are indirectly evaluated using the rigid body motion method. In fact, strong-singular integrals consistently contribute to the diagonal elements of the displacement coefficient matrix [H]. If assuming that the displacements of all nodes are 1 in the computational domain, the strains, stresses, and surface tractions all equal to 0. This implies that if adding all the elements of any row in matrix [H], the result must be zero.

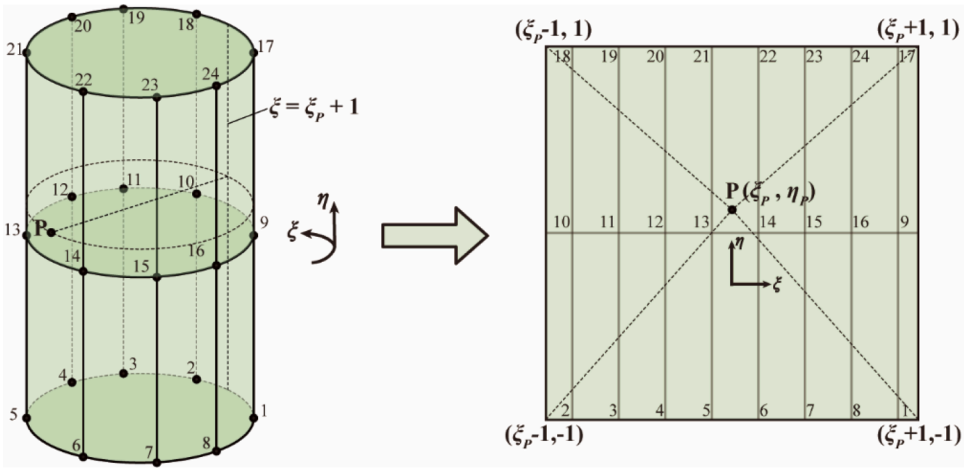

Fig. 13. Mapping a tube element to the intrinsic parameter space.

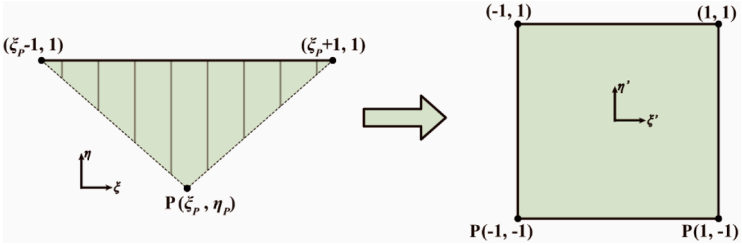

Fig. 14. Mapping a triangle to a square element.

So, the diagonal of matrix [H] can be calculated by the following formula:

$$[H]_{ii} = -\sum_{k=1,k\neq i}^{N} [H]_{ik} \tag{30}$$

where N is the number of elements in the i th row of [H]. Of course, it can be easily found that this method also eliminates the need to determine the coefficient c in Eq.(1), which originally involves the geometric information of the computational domain.

4.3. Nearly singular integral

When the source point is not located on the element, it seems that no singularity problem needs to be concerned. However, when the source point is close to the element, the terms r^{-1}, r^{-2} or $\ln(r^{-1})$ in the integrands change drastically, which possibly makes Gauss-Legendre quadrature inaccurate. In this paper, nearly weak-, strong- and hyper-singular integrals are all treated by adaptive element sub-division method [23]. To implement this method, it is necessary to define what "close" means first. In this paper, the nearly singularity will be concerned if the distance from the source point to the element (represented by $r_{\min}$) satisfies the following formula [5]:

$$r_{\min} \leq \frac{L_i}{4}\left(\frac{e}{2}\right)^{-p/(2m_i)} \tag{31}$$

in which L_i represents the element real length along the i th direction and can be easily obtained by integration with few Gauss points; e is the predetermined upper limit of integral errors using Gauss-Legendre quadrature formula; m_i is the predetermined maximum number of Gauss points along the i th direction; p is determined by the singularity order λ of the integrand, which can be expressed as follows:

$$p = \sqrt{\frac{2}{3}\lambda + \frac{2}{5}} \tag{32}$$

The second problem is to determine $r_{\min}$, from the source point to an element, which can be in any position. In this paper, the Newton iteration method is applied. The iteration begins with an initial estimate of the point on the element that is closest to the source point, whose intrinsic coordinate is represented by ξ. The iterative increment $\Delta\xi$ can be obtained by solving the following equation:

$$\left(\frac{\partial x_i}{\partial \xi}\cdot\frac{\partial x_i}{\partial \xi} + r_i\cdot\frac{\partial^2 x_i}{\partial \xi^2}\right)\Delta\xi = -r_i\cdot\frac{\partial x_i}{\partial \xi} \tag{33}$$

in which the repeated subscripts i imply summations, which range from 1 to 2 for 2D problems and from 1 to 3 for 3D problems; r_i signifies distance along the i th orientation from the source point to the guessed point. For the hole elements or the first dimension of tube elements, the results may converge at the maximum distance because the essence of the Newton iteration is to identify a stationary point of the distance function. Therefore, after the iteration converges at intrinsic coordinate ξ, it is necessary to compare the distance from the source point to the coordinate $\xi + 1$ or $\xi - 1$, with ξ. The shorter one is the minimum distance.

The main idea of element sub-division is to divide the element into several sub-elements to decrease L for adhering to the principle outlined in Eq.(30). This principle can also be transformed into another form for obtaining the length of each sub-element:

$$L_i = 4r\left(\frac{e}{2}\right)^{p/(2m_i)} \tag{34}$$

where r represents the minimum distance from the source point to the sub-element, and it would be changed as the element is sub-divided successively. The process of element sub-division unfolds as follows:

1) Calculate the length L_i of the element. Get the minimum distance $r_{\min}$ and intrinsic coordinate of the minimum distance point A. Meanwhile, record the intrinsic coordinate of the maximum distance point B.
2) Based on L_i and $r_{\min}$, judge if the Eq.(30) is true. If it does not, there is no need to sub-divide this element in term of this source point along the i th direction. If it is true, continue the element sub-division procedure.
3) In case of the hole elements or the first dimension of tube elements, sub-division process should always be implemented along two orientations, spanning from the minimum distance point A to the maximum distance point B, as shown in Fig. 15. For the second dimension of tube elements, sub-division process should be implemented in the intervals $[-1, \eta_P]$ and $[\eta_P, 1]$. Within each sub-division interval, set $r_{\min}$ be r, calculate L_{i1} and identify the first sub-division point.
4) In each sub-division interval, ascertain the distance between the source point P and the latest sub-division point, denoted as r_n. Set r_n be r, calculate L_{in}, which signifies the length of the n-th sub-element, and identify the next sub-division point. If the intrinsic coordinate of this point exceeds the maximum distance point B or the boundary of this direction, terminate the sub-division process along the i th direction.

Fig. 15 shows possible sub-division results of a hole element and a tube element.

5. Numerical examples

To compare the robustness of Lagrange and trigonometric hole elements and verify the correctness of the techniques about the hole and tube elements, five numerical examples are implemented in this section.

5.1. Plate with single small hole

The first example, a 100×100 square plate with a hole of radius 1 in the center is considered. For convenience, the origin of the coordinate system is set at the center of the hole, with the $\boldsymbol{x}$ and $\boldsymbol{y}$ axes aligned parallel to the plate's edges, as shown in Fig. 16. Four boundaries of the plate are subjected to the surface tractions, of which the distributions are determined by the following formula:

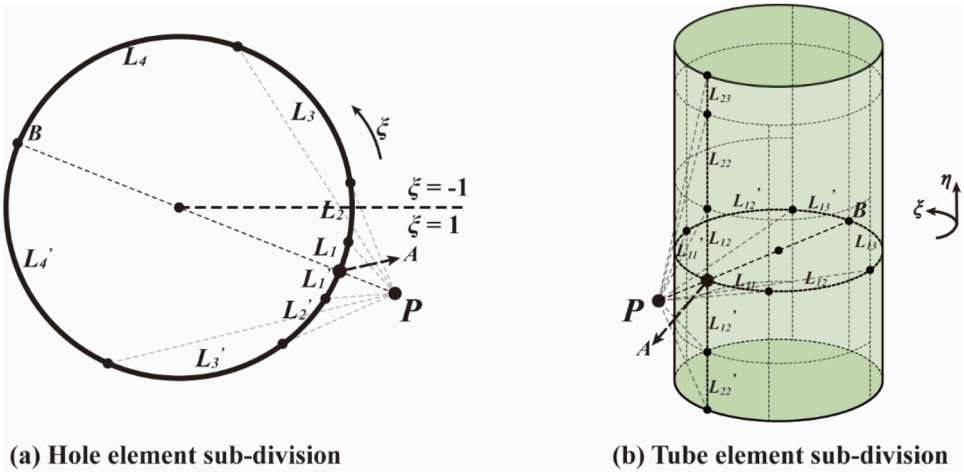

Fig. 15. Adaptive element sub-division for a hole element and a tube element.

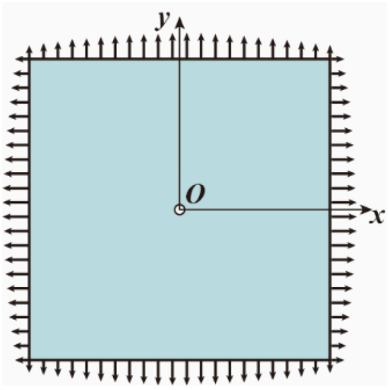

Fig. 16. The coordinate system and boundary conditions of Example 1.

$$\begin{cases} t_1 = \sigma_{11} n_1 + \sigma_{12} n_2 \\ t_2 = \sigma_{21} n_1 + \sigma_{22} n_2 \end{cases} \tag{35}$$

in which $\boldsymbol{n} = (n_1, n_2)$ denotes the outward normal vector of the boundaries; $\boldsymbol{t} = (t_1, t_2)$ is the surface traction on the boundaries; the components of stresses are calculated by:

$$\begin{cases} \sigma_{11} = \dfrac{qx^2}{x^2+y^2}\left(1-\dfrac{R^2}{x^2+y^2}\right) + \dfrac{qy^2}{x^2+y^2}\left(1+\dfrac{R^2}{x^2+y^2}\right) \\ \sigma_{22} = \dfrac{qy^2}{x^2+y^2}\left(1-\dfrac{R^2}{x^2+y^2}\right) + \dfrac{qx^2}{x^2+y^2}\left(1+\dfrac{R^2}{x^2+y^2}\right) \\ \sigma_{12} = \sigma_{21} = -\dfrac{2qxyR^2}{\left(x^2+y^2\right)^2} \end{cases} \tag{36}$$

in which $q = 1$ in this example; R represents the radius of the hole and equals 1. Consequently, the stress distributions over the entire plate are the same as the Eq.(35), and the von-Mises stress can be written as follows:

$$\sigma_{mises} = \sqrt{1 + \frac{3R^4}{\left(x^2+y^2\right)^2}} \tag{37}$$

This stress distribution is the same as that of the infinite plate with a circular hole.

For the sake of comparison, an FEM model and several BEM models are established. FEM model contains 1360 8-node elements and 4192 nodes with 64 nodes uniformly distributed around the hole, as depicted in Fig. 17(a). In all BEM models, 80 quadratic line elements are uniformly distributed along four edges of plate, matching the interpolation accuracy of the FEM model. However, there are 30 different approaches to discretizing the central hole within these BEM models. This includes discretization using 4, 8, 32 quadratic line elements, 3, 4, 6, 8, 12, 16-node trigonometric hole elements, and 10–3, 16–3, 22–3, 28–3, 5–4, 9–4, 13–4, 17–4, 21–4, 25–4, 7–6, 13–6, 19–6, 25–6, 9–8, 17–8, 25–8,

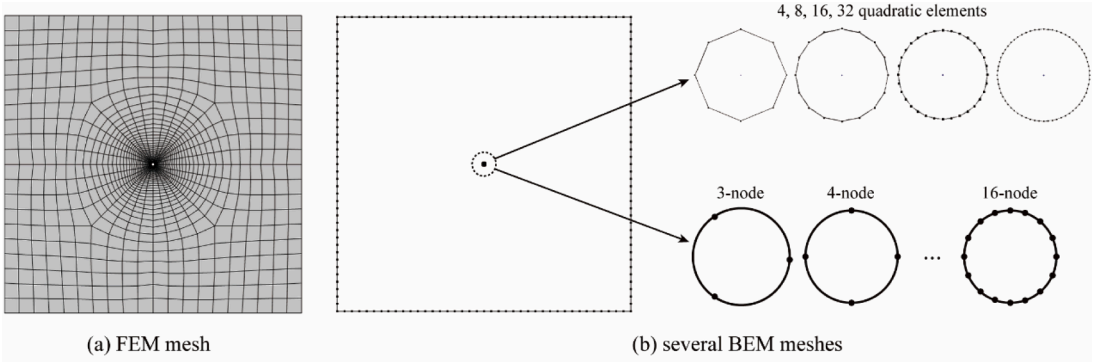

Fig. 17. FEM model and BEM model with conventional boundary element.

Table 1
The maximum errors on the circular hole ("BEM-4 quadratic" means 4 quadratic elements are used to discretize the hole; "BEM-10–3-Lag.-hole" means only one 10–3 Lagrange hole element is used to discretize the hole; "BEM-3n-tri.-hole" means only one 3-node trigonometric hole element is used to discretize the hole and so on.).

Discretization method	error	Discretization method	error	Discretization method	error
FEM	5.807%	BEM-13–4-Lag.-hole	0.212%	BEM-17–8-Lag.-hole	0.014%
BEM-4 quadratic	2.367%	BEM-17–4-Lag.-hole	0.037%	BEM-25–8-Lag.-hole	0.014%
BEM-8 quadratic	0.109%	BEM-21–4-Lag.-hole	0.007%	BEM-8n-tri.-hole	0.014%
BEM-32 quadratic	0.014%	BEM-25–4-Lag.-hole	0.004%	BEM-13–12-Lag.-hole	0.012%
BEM-10–3-Lag.-hole	10.78%	BEM-4n-tri.-hole	0.003%	BEM-25–12-Lag.-hole	0.274%
BEM-16–3-Lag.-hole	3.966%	BEM-7–6-Lag.-hole	6.807%	BEM-12n-tri.-hole	0.013%
BEM-22–3-Lag.-hole	1.478%	BEM-13–6-Lag.-hole	0.025%	BEM-17–16-Lag.-hole	0.075%
BEM-28–3-Lag.-hole	0.561%	BEM-19–6-Lag.-hole	0.013%	BEM-33–16-Lag.-hole	1.314%
BEM-3n-tri.-hole	0.013%	BEM-25–6-Lag.-hole	0.013%	BEM-16-n-tri.-hole	0.014%
BEM-5–4-Lag.-hole	9.734%	BEM-6n-tri.-hole	0.013%		
BEM-9–4-Lag.-hole	1.285%	BEM-9–8-Lag.-hole	0.617%		

13–12, 25–12, 17–16, 33–16 Lagrange hole elements.

Following computation, the von-Mises stresses of the nodes on the hole are extracted. Compared with the benchmark (the exact stress distribution in this example), the stress errors are calculated by the following formula:

$$error = \left| \frac{\sigma - \sigma_B}{\sigma_{\max} - \sigma_{\min}} \right| \times 100\% \tag{38}$$

in which σ is the calculated stress; σ_B is the stress of benchmark (either the exact solution or the results of the refined mesh); $\sigma_{\max}$ is the maximum stress over the entire computational domain of the benchmark, while $\sigma_{\min}$ is the minimum one, and $\sigma_{\max}$ - $\sigma_{\min}$ represents the range of stress of the benchmark. The maximum error among the extracted nodes of each model is documented in Table 1. Some conclusions are drawn as follows.

- It can be found that when simulating the effect of stress concentration around small holes, conventional BEM performs better than FEM, when they share the same interpolation order and the same number of nodes on the boundary (as observed in "FEM" and "BEM-32 quadratic" in Table 1).
- Compared Lagrange and trigonometric hole elements with the same number of nodes, trigonometric elements perform as well as or better than Lagrange element.
- From the errors of all the Lagrange hole elements, when the number of nodes is not greater than 8, employing more auxiliary nodes can lead to higher accuracy. However, in the case of 12-node or 16-node Lagrange hole elements, more auxiliary nodes may lead to lower accuracy. The authors believe this may result from Runge phenomenon associated with Lagrange interpolation.
- In the context of a plate with single small hole, 3-node trigonometric hole element provides nearly equivalent accuracy to that of 32 quadratic line elements (with 64 nodes on the hole) when simulating a circular hole, This highlights the advantage of the trigonometric hole element.

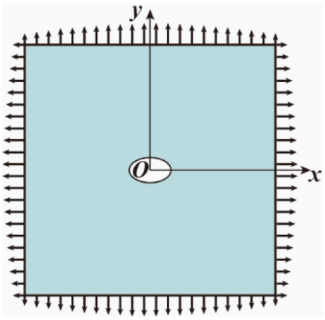

Fig. 18. The computational model of Example 2.

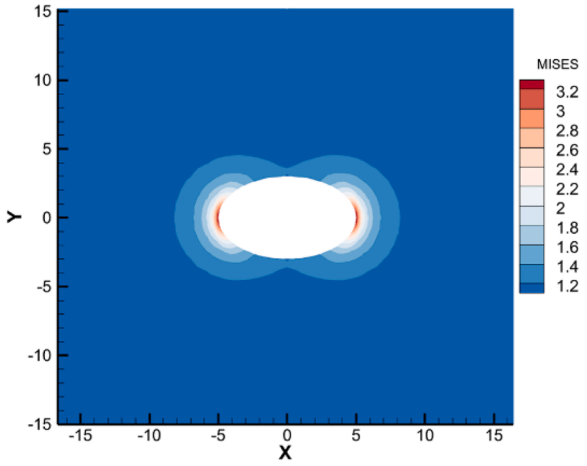

Fig. 19. Von-Mises stress contour around the elliptic hole.

5.2. Plate with elliptical holes

The second example closely resembles the first one, with the sole difference being the substitution of the circular hole with an elliptic hole having a semi-major axis of 5 and a semi-minor axis of 3, as depicted in Fig. 18. Due to the alteration in geometry, it is not straightforward to obtain an exact stress solution. Therefore, a highly refined BEM mesh is used to calculate this problem, yielding results accurate enough to serve as benchmarks. Fig. 19 displays a segment of the von-Mises stress contour around the elliptic hole. Meanwhile, 30 kinds of BEM discretization methods over the hole are calculated. In this example, some of the hole elements are tested with two node distribution methods: angle-middle and arc-middle. It should be noticed that the hole discretized by several quadratic line elements are all arc-middle distribution, based on prior experiences.

Following the calculations, the maximum errors on the elliptic holes of all meshes are listed in Table 2 and Table 3, corresponding to angle-middle and arc-middle node distribution, respectively. When observing the overall performance of these hole elements in simulating elliptic holes, the results are generally consistent with those of circular holes. Some conclusions are summarized as follows.

- When using the hole element to simulate the elliptic geometries, angle-middle node distributions are superior to arc-middle node distributions for both trigonometric and Lagrange hole elements.
- When simulating the elliptic hole, all the trigonometric hole element and 17–4, 21–4, 25–4, 13–6, 19–6, 25–6, 17–8, 25–8 Lagrange hole elements are recommended. For 6-node hole element, 19–6, 25–6 Lagrange hole element even perform better than trigonometric.

Table 2
The maximum errors on the elliptic hole with angle-middle node distribution.

Discretization method	error	Discretization method	error	Discretization method	error
BEM-10–3-Lag.-hole	18.63%	BEM-21–4-Lag.-hole	0.005%	BEM-17–8-Lag.-hole	0.003%
BEM-16–3-Lag.-hole	5.683%	BEM-25–4-Lag.-hole	0.002%	BEM-25–8-Lag.-hole	0.001%
BEM-22–3-Lag.-hole	1.963%	BEM-4n-tri.-hole	0.001%	BEM-8n-tri.-hole	< 0.001%
BEM-28–3-Lag.-hole	0.730%	BEM-7–6-Lag.-hole	6.781%	BEM-13–12-Lag.-hole	0.004%
BEM-3n-tri.-hole	0.001%	BEM-13–6-Lag.-hole	0.008%	BEM-25–12-Lag.-hole	0.753%
BEM-5–4-Lag.-hole	9.001%	BEM-19–6-Lag.-hole	< 0.001%	BEM-12n-tri.-hole	< 0.001%
BEM-9–4-Lag.-hole	0.819%	BEM-25–6-Lag.-hole	< 0.001%	BEM-17–16-Lag.-hole	2.987%
BEM-13–4-Lag.-hole	0.118%	BEM-6n-tri.-hole	0.001%	BEM-33–16-Lag.-hole	46.79%
BEM-17–4-Lag.-hole	0.021%	BEM-9–8-Lag.-hole	0.509%	BEM-16n-tri.-hole	< 0.001%

Table 3
The maximum errors on the elliptic hole with arc-middle node distribution.

Discretization method	error	Discretization method	error	Discretization method	error
BEM-4 quadratic	35.16%	BEM-9–8-Lag.-hole	41.66%	BEM-17–16-Lag.-hole	92.90%
BEM-8 quadratic	11.03%	BEM-17–8-Lag.-hole	3.908%	BEM-33–16-Lag.-hole	84.09%
BEM-16 quadratic	2.765%	BEM-25–8-Lag.-hole	1.186%	BEM-16n-tri.-hole	0.016%
BEM-32 quadratic	0.002%	BEM-8n-tri.-hole	0.056%		

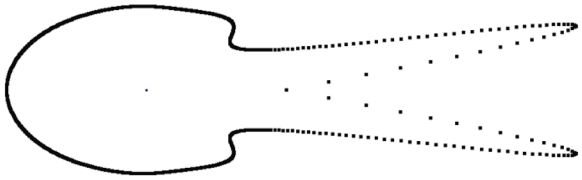

Fig. 20. Result of simulating the elliptic hole by 17–16 Lagrange hole element.

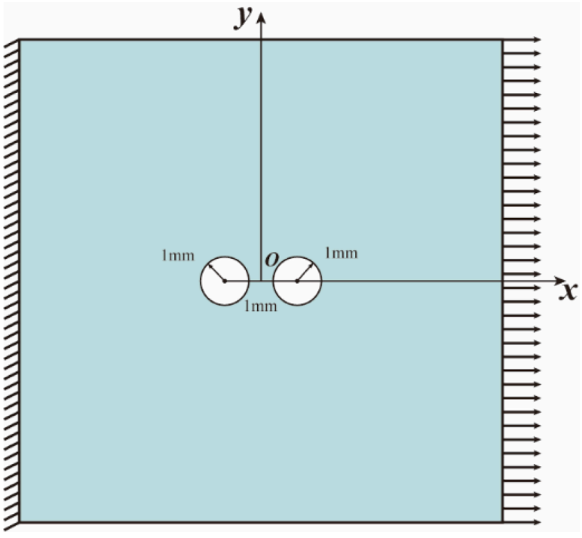

Fig. 21. The computational model of Example 3.

- The von-Mises stress results for 17–16 and 33–16 Lagrange hole elements are unreliable when simulating elliptical holes, regardless of whether arc-middle or angle-middle node distribution is used. Fig. 20 displays the geometric representation of an elliptical hole using the 17–16 Lagrange hole element with arc-middle node distribution. It is obvious that the Runge phenomenon emerges during the interpolation of elliptical geometries. So, it can be inferred that the interpolation of physical variables also appears Runge phenomenon, contributing to the significant simulation errors.

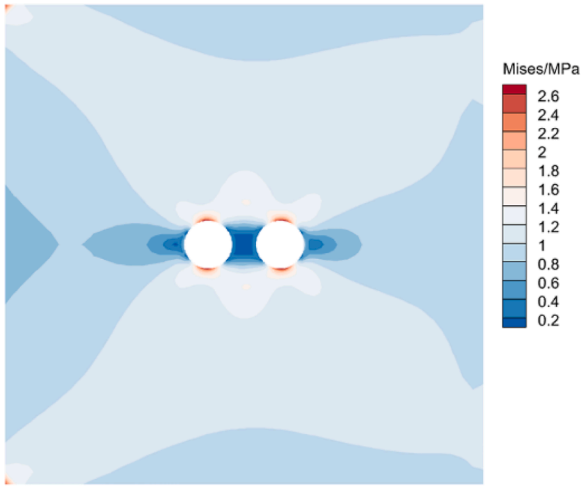

Fig. 22. Von-Mises stress contour of the plate with two holes.

5.3. *Plate with double holes*

The third example considers a 20mm×20 mm square plate with two holes of radius 1. Fig. 21 displays the hole positions, the coordinate system, and the boundary conditions. Two holes are symmetrically distributed on the left and right of the plate center, with their centers positioned 1.5 mm away from the plate center. Obviously, the stress distributions will be influenced by the interaction between the two holes. The right edge of the plate is subjected to uniformly distributed traction of 1 MPa, while the left edge is fixed. Due to the difficulty in obtaining an exact solution for this problem, a highly refined BEM mesh is employed to calculate it. The results are considered as the benchmarks, and the von-Mises stress contour is depicted in Fig. 22. In the case of other BEM meshes, four edges of the square plate are all discretized by 178 quadratic line elements. The two holes are discretized differently, with options including 3, 4, 6, 8, 12, 16-node trigonometric hole elements and 4, 8, 16, 32 quadratic line elements, respectively, for different kinds of meshes. In addition, to show the effect of near-singular integrals, the model with 16-node trigonometric hole elements is also calculated without employing any special treatment for near-singularity on the holes.

Following the calculations, the maximum errors on the left hole of all the meshes are documented in the Table 4. In the case of the model using

Table 4
The maximum errors on the left hole of all kinds of meshes.

Discretization method	error	Discretization method	error	Discretization method	error
4 quadratic elements	8.236%	8 quadratic elements	2.152%	16 quadratic elements	0.791%
32 quadratic elements	0.244%	3-node trigonometric	23.107%	4-node trigonometric	14.826%
6-node trigonometric	7.721%	8-node trigonometric	3.108%	12-node trigonometric	0.444%
16-node trigonometric	0.070%				

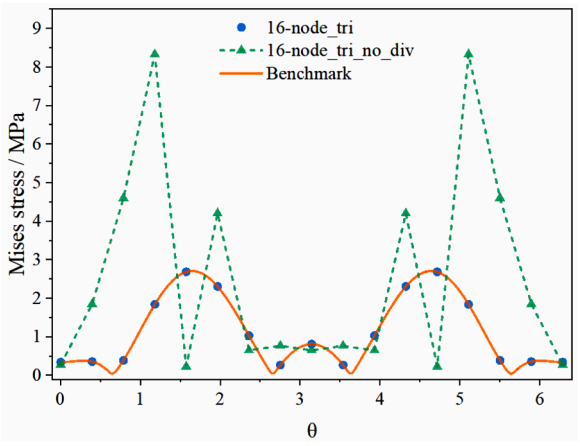

Fig. 23. Von-Mises stresses on the left holes of all kinds of meshes.

16-node hole elements, the von-Mises stresses on the left holes are extracted and plotted in Fig. 23, where the green dotted line with triangular points represents the results without special treatment of near-singularity on the hole elements, while the blue round points represent the results achieved by evaluating near-singular integrals on the holes using the proposed element sub-division method. The orange line represents the benchmark. Several observations are summarized as follows.

- In terms of maximum errors of von-Mises stress on the left hole, the order is as follows: one 16-node hole element < 32 quadratic elements (64 nodes) < one 12-node hole element < 16 quadratic elements (32 nodes) < 8 quadratic elements (16 nodes) < one 8-node hole element. This suggests that using trigonometric hole elements for hole simulation can reduce the number of the nodes in the same accuracy requirement.
- It appears that 3, 4 and 6-node trigonometric hole element are unable to accurately capture the variations of stresses over left holes due to the absence of higher-order trigonometric bases. It is imperative to expand the trigonometric hole elements to 8-node, 12-node, and 16-node versions for problems involving closely spaced holes.

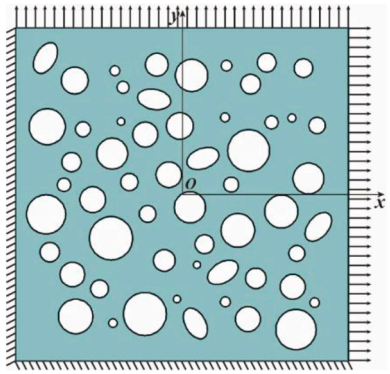

Fig. 24. The computational model of Example 4.

- Since the two holes are in close proximity, near-singular integrals over them require special treatment. The results indicate that the proposed sub-division method over hole elements can evaluate these near-singular integrals accurately.

5.4. Plate with randomly distributed holes

The fourth example considers a 100×100 plate with a total of 50 circular holes and 6 elliptic holes. The positions and sizes of these holes are randomly generated, as illustrated in Fig. 24.The radii of the circular holes vary from 1 to 7. The minimum distance between any two holes is set to 2.0. The upper and right side of the plate is subjected to a uniformly distributed traction of 0.2, while the left and lower side is fixed. A highly refined BEM mesh is utilized as the benchmark. This mesh consists of 320 quadratic elements along the four edges and 64 quadratic elements surrounding each hole. In other meshes, four edges are discretized by 160 quadratic line elements. The holes are discretized differently, with options including 8-node and 16-node trigonometric hole elements, as well as 4, 8, 16, or 32 quadratic elements.

After calculation, von-Mises stresses on the nodes located at all the holes are extracted. Both the maximum errors and the average errors are evaluated and listed in the Table 5. Meanwhile, von-Mises stress contours for both the refined mesh and the mesh with 16-node hole elements are displayed in Fig. 25. From Table 5, some conclusions are summarized as follows.

- In terms of the maximum errors, the hierarchy is as follows: 32 quadratic elements (64 nodes) < 16 quadratic elements (32 nodes) < one 16-node hole element < 8 quadratic elements (16 nodes) < one 8-node hole element < 4 quadratic elements (8 nodes). It can be concluded that using the trigonometric hole element is better than using several quadratic elements, in the premise of the same number of nodes on the hole.
- In this example, the 8-node hole element exhibits a relatively large maximum error. It seems that 8-node hole element is unable to accurately simulate the circumferential stress variation of some holes which are located in close proximity to other holes. Combining this observation with the findings in the third example, it can be inferred that when two holes are in close proximity, a greater number of nodes in the hole element is required to accurately simulate the stress concentration effect.

5.5. Cube with a cylindrical hole

The fifth example considers a cube with a cylindrical hole, as is shown in Fig. 26, to demonstrate the advantages of the tube element. The cube has an edge length of 10, and the cylindrical hole has a radius of 1. The surface with its outward normal along the positive x-axis is subjected to a uniformly distributed traction of 1, while the surface with its outward normal along the negative x-axis is fixed. A refined mesh with 10,824 8-node quadratic elements is employed. The stress results from this mesh are regarded as benchmarks, and the stress contour is shown in Fig. 27. Besides, four types of meshes are used, with each of four lateral surfaces discretized by 10×10 8-node elements. The cylindrical hole is discretized by four different configurations: 32×10, 16×10, 8 × 10 8-node quadratic elements, as well as 10 24-node tube elements (shown in Fig. 12). Four kinds of meshes are shown in Fig. 28.

Table 5
The maximum errors and the average errors of all the kinds of meshes.

Discretization method	Max. error	Average error	Discretization method	Max. error	Average error
4 quadratic elements	11.24%	1.379%	8 quadratic elements	5.153%	0.434%
16 quadratic elements	1.564%	0.138%	32 quadratic elements	0.609%	0.040%
8-node trigonometric	8.637%	0.856%	16-node trigonometric	2.242%	0.093%

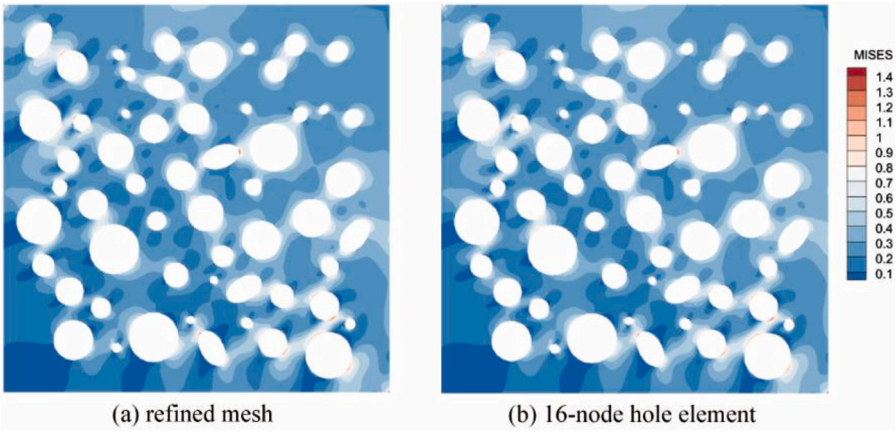

Fig. 25. Von-Mises stress contours of two meshes.

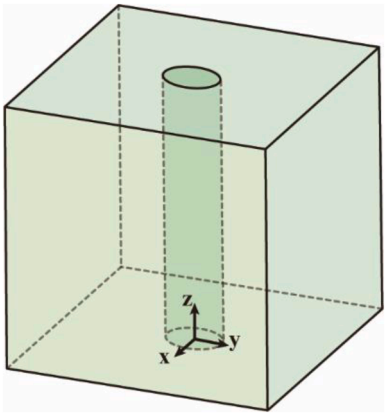

Fig. 26. The model of the fifth example.

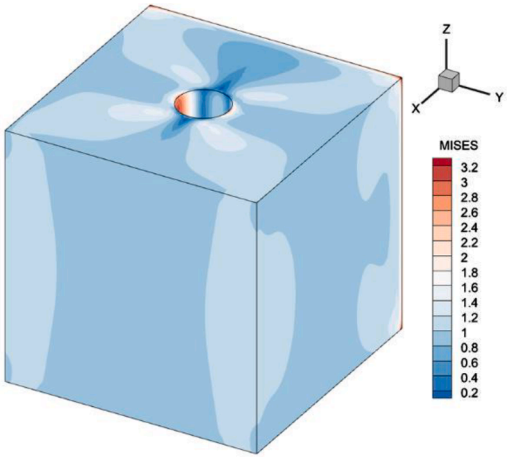

Fig. 27. The contour plot over the refined mesh.

The stresses of the nodes on the cylindrical hole are extracted. The Mises stress contours over the cylinders of the refined mesh and the mesh with 10 24-node tube elements are shown in Fig. 29(a) and (b), respectively. And the maximum stress errors among these nodes of four kinds of meshes are listed in Table 6. The stress errors along the line $x = 0$, $y = 1$ (a generatrix of the cylinder) of four meshes are plotted in Fig. 30. From the table and the figure, it can be concluded that 10 24-node tube elements, despite having fewer nodes, perform better than 320 quadratic elements in simulating the cylindrical hole. In the event of numerous cylindrical holes within a 3D model, opting for tube elements may be a more suitable choice. Meanwhile, it can be found that stress errors are large at two ends of the cylindrical hole. In general, more elements should be distributed there, which is not done here for straightforward comparison (Fig. 31).

6. Conclusion

In this paper, the construction methods of "repeated winding" Lagrange hole elements, trigonometric hole elements with varying number of nodes, and the corresponding tube elements are introduced. Meanwhile, the adaptive element sub-division method is expanded to both hole elements and tube elements to deal with the near-singularity. In the last section of the paper, five numerical examples are implemented by using the proposed elements. The following concluding remarks can be drawn.

- The sub-division processes for the hole elements and the first dimension of the tube elements should always be implemented along two orientations, both extending from the minimum distance point to the maximum distance point.
- For a - b Lagrange hole element, if b (the number of nodes in the hole element) is 3, 4, 6 or 8, greater values of a (the number of nodes in the original line element) lead to higher accuracy, no matter for the accuracy of geometry or physical quantity. However, when b is 12 or 16, the accuracy may be compromised due to the Runge phenomenon of Lagrange interpolation.
- Trigonometric hole elements perform as well as or better than Lagrange hole elements when simulating circular or elliptic holes in most cases.

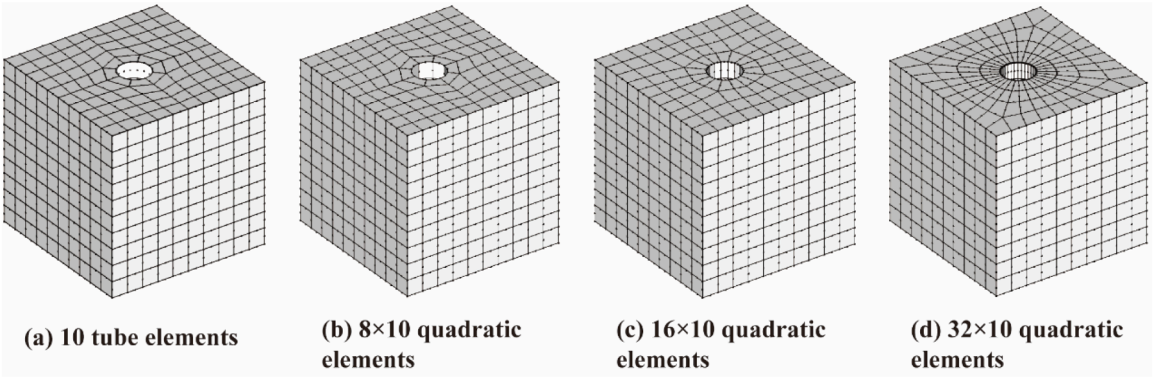

Fig. 28. Four kinds of meshes for cube with cylindrical hole.

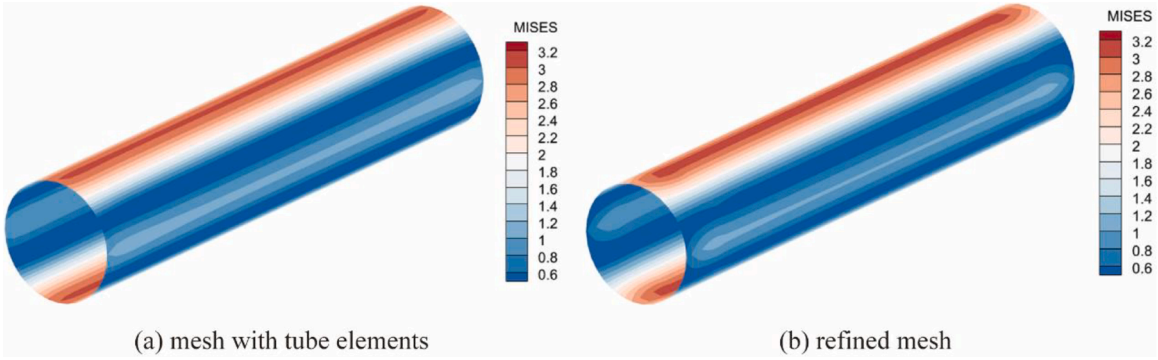

Fig. 29. Von-Mises stress contours over the cylinder.

Table 6
The maximum errors of all the kinds of meshes in example 5.

Discretization	Total number of nodes in model	Max. error
10 24-node tube elements	2144	0.283%
32×10 quadratic elements	2952	0.310%
16×10 quadratic elements	2280	1.147%
8 × 10 quadratic elements	2064	3.663%

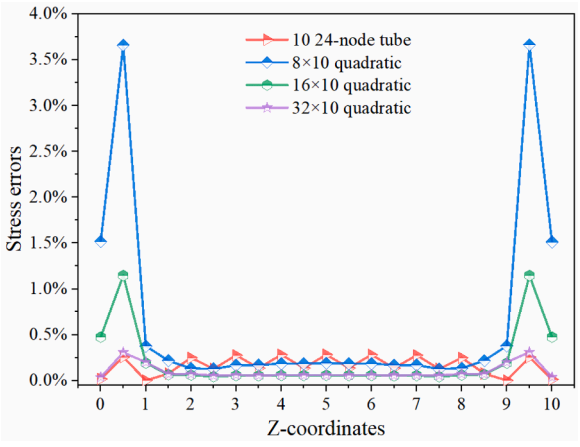

Fig. 30. Von-Mises stress errors along the line $x = 0$, $y = 1$ of four meshes.

- When two or more holes interfere with each other, low order hole elements such as 3, 4 or 6-node element, may not provide sufficient accuracy to depict the stress concentration over the holes. For these cases, 8, 12, or even 16-node trigonometric hole elements should be employed.
- Compared with using several quadratic elements, using hole elements or tube elements to simulate the stresses over the holes or cylindrical holes can reduce the number of nodes required to meet the same accuracy standards.
- When using the hole elements to simulate elliptic geometries, angle-middle node distributions yield better results than arc-middle node distributions, especially for Lagrange hole elements.

The hole elements and tube elements are the base of the ring element, disk element and sphere element, of which the node distributions, singular integrals, applicability and so on can be further studied in the future.

Data availability

The raw/processed data required to reproduce these findings cannot be shared at this time as the data also forms part of an ongoing study.

Declaration of Competing Interest

The authors declare that they have no competing of interests.

Acknowledgement

The support of this investigation by the National Natural Science Foundation of China (Grant Nos. 12302261, 12072064, 12272081, 11972179) are gratefully acknowledged.

Appendix A. The shape functions and diagrams of trigonometric hole elements

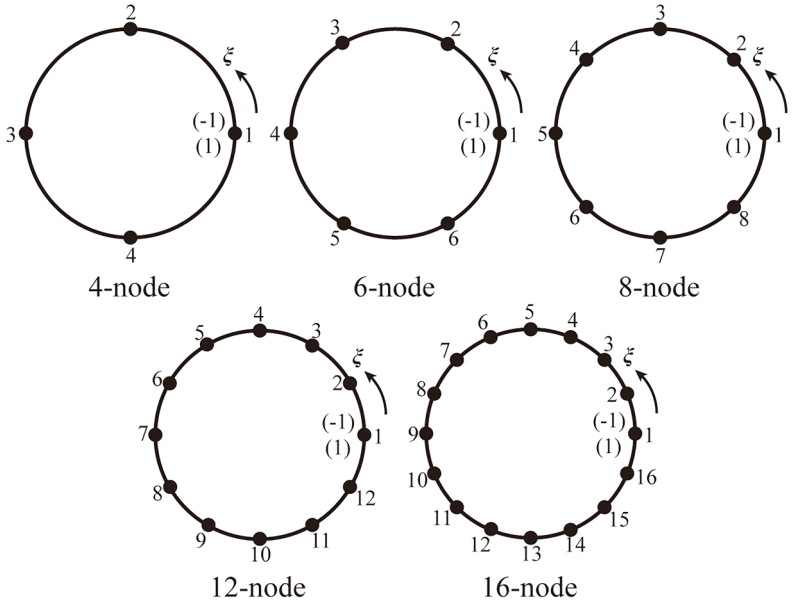

Fig. 31. The diagrams of 4, 6, 8, 12, 16-node trigonometric hole element.

4-node hole element:

$$N_1(\theta)=\frac{1}{2}\cos\theta+\frac{1}{2}\cos^2\theta$$

$$N_2(\theta)=\frac{1}{2}+\frac{1}{2}\sin\theta-\frac{1}{2}\cos^2\theta$$

$$N_3(\theta)=-\frac{1}{2}\cos\theta+\frac{1}{2}\cos^2\theta$$

$$N_4(\theta)=\frac{1}{2}-\frac{1}{2}\sin\theta-\frac{1}{2}\cos^2\theta$$

6-node hole element:

$$N_1(\theta)=-\frac{1}{6}-\frac{1}{6}\cos\theta+\frac{2}{3}\cos^2\theta+\frac{2}{3}\cos^3\theta$$

$$N_2(\theta)=\frac{1}{3}+\frac{2}{3}\cos\theta-\frac{1}{3}\cos^2\theta-\frac{2}{3}\cos^3\theta+\left(\frac{\sqrt{3}}{6}+\frac{\sqrt{3}}{3}\cos\theta\right)\sin\theta$$

$$N_3(\theta)=\frac{1}{3}-\frac{2}{3}\cos\theta-\frac{1}{3}\cos^2\theta+\frac{2}{3}\cos^3\theta+\left(\frac{\sqrt{3}}{6}-\frac{\sqrt{3}}{3}\cos\theta\right)\sin\theta$$

$$N_4(\theta)=-\frac{1}{6}+\frac{1}{6}\cos\theta+\frac{2}{3}\cos^2\theta-\frac{2}{3}\cos^3\theta$$

$$N_5(\theta)=\frac{1}{3}-\frac{2}{3}\cos\theta-\frac{1}{3}\cos^2\theta+\frac{2}{3}\cos^3\theta+\left(-\frac{\sqrt{3}}{6}+\frac{\sqrt{3}}{3}\cos\theta\right)\sin\theta$$

$$N_6(\theta)=\frac{1}{3}+\frac{2}{3}\cos\theta-\frac{1}{3}\cos^2\theta-\frac{2}{3}\cos^3\theta+\left(-\frac{\sqrt{3}}{6}-\frac{\sqrt{3}}{3}\cos\theta\right)\sin\theta$$

8-node hole element:

$$N_1(\theta)=-\frac{1}{2}\cos\theta-\frac{1}{2}\cos^2\theta+\cos^3\theta+\cos^4\theta$$

$$N_2(\theta)=\frac{\sqrt{2}}{2}\cos\theta+\cos^2\theta-\frac{\sqrt{2}}{2}\cos^3\theta-\cos^4\theta+\left(\frac{1}{2}\cos\theta+\frac{\sqrt{2}}{2}\cos^2\theta\right)\sin\theta$$

$$N_3(\theta)=\frac{1}{2}-\frac{3}{2}\cos^2\theta+\cos^4\theta+\left(\frac{1}{2}-\cos\theta\right)\sin\theta$$

$$N_4(\theta)=-\frac{\sqrt{2}}{2}\cos\theta+\cos^2\theta+\frac{\sqrt{2}}{2}\cos^3\theta-\cos^4\theta-\left(\frac{1}{2}\cos\theta-\frac{\sqrt{2}}{2}\cos^2\theta\right)\sin\theta$$

$$N_5(\theta)=\frac{1}{2}\cos\theta-\frac{1}{2}\cos^2\theta-\cos^3\theta+\cos^4\theta$$

$$N_6(\theta)=-\frac{\sqrt{2}}{2}\cos\theta+\cos^2\theta+\frac{\sqrt{2}}{2}\cos^3\theta-\cos^4\theta+\left(\frac{1}{2}\cos\theta-\frac{\sqrt{2}}{2}\cos^2\theta\right)\sin\theta$$

$$N_7(\theta)=\frac{1}{2}-\frac{3}{2}\cos^2\theta+\cos^4\theta+\left(-\frac{1}{2}+\cos\theta\right)\sin\theta$$

$$N_8(\theta)=\frac{\sqrt{2}}{2}\cos\theta+\cos^2\theta-\frac{\sqrt{2}}{2}\cos^3\theta-\cos^4\theta-\left(\frac{1}{2}\cos\theta+\frac{\sqrt{2}}{2}\cos^2\theta\right)\sin\theta$$

12-node hole element:

$$N_1(\theta)=\frac{1}{2}\cos\theta+\frac{1}{2}\cos^2\theta-\frac{8}{3}\cos^3\theta-\frac{8}{3}\cos^4\theta+\frac{8}{3}\cos^5\theta+\frac{8}{3}\cos^6\theta$$

$$N_2(\theta)=-\frac{\sqrt{3}}{3}\cos\theta-\frac{2}{3}\cos^2\theta+\frac{5\sqrt{3}}{3}\cos^3\theta+\frac{10}{3}\cos^4\theta-\frac{4\sqrt{3}}{3}\cos^5\theta$$
$$-\frac{8}{3}\cos^6\theta+\left(-\frac{\sqrt{3}}{6}\cos\theta-\frac{1}{3}\cos^2\theta+\frac{2\sqrt{3}}{3}\cos^3\theta+\frac{4}{3}\cos^4\theta\right)\sin\theta$$

$$N_3(\theta)=\cos\theta+2\cos^2\theta-\frac{7}{3}\cos^3\theta-\frac{14}{3}\cos^4\theta+\frac{4}{3}\cos^5\theta+\frac{8}{3}\cos^6\theta$$
$$+\left(\frac{\sqrt{3}}{2}\cos\theta+\sqrt{3}\cos^2\theta-\frac{2\sqrt{3}}{3}\cos^3\theta-\frac{4\sqrt{3}}{3}\cos^4\theta\right)\sin\theta$$

$$N_4(\theta)=\frac{1}{2}-\frac{19}{6}\cos^2\theta+\frac{16}{3}\cos^4\theta-\frac{8}{3}\cos^6\theta+\left(\frac{1}{2}-\frac{8}{3}\cos^2\theta+\frac{8}{3}\cos^4\theta\right)\sin\theta$$

$$N_5(\theta)=-\cos\theta+2\cos^2\theta+\frac{7}{3}\cos^3\theta-\frac{14}{3}\cos^4\theta-\frac{4}{3}\cos^5\theta+\frac{8}{3}\cos^6\theta$$
$$+\left(-\frac{\sqrt{3}}{2}\cos\theta+\sqrt{3}\cos^2\theta+\frac{2\sqrt{3}}{3}\cos^3\theta-\frac{4\sqrt{3}}{3}\cos^4\theta\right)\sin\theta$$

$$N_6(\theta)=\frac{\sqrt{3}}{3}\cos\theta-\frac{2}{3}\cos^2\theta-\frac{5\sqrt{3}}{3}\cos^3\theta+\frac{10}{3}\cos^4\theta+\frac{4\sqrt{3}}{3}\cos^5\theta$$
$$-\frac{8}{3}\cos^6\theta+\left(\frac{\sqrt{3}}{6}\cos\theta-\frac{1}{3}\cos^2\theta-\frac{2\sqrt{3}}{3}\cos^3\theta+\frac{4}{3}\cos^4\theta\right)\sin\theta$$

$$N_7(\theta)=-\frac{1}{2}\cos\theta+\frac{1}{2}\cos^2\theta+\frac{8}{3}\cos^3\theta-\frac{8}{3}\cos^4\theta-\frac{8}{3}\cos^5\theta+\frac{8}{3}\cos^6\theta$$

$$N_8(\theta)=\frac{\sqrt{3}}{3}\cos\theta-\frac{2}{3}\cos^2\theta-\frac{5\sqrt{3}}{3}\cos^3\theta+\frac{10}{3}\cos^4\theta+\frac{4\sqrt{3}}{3}\cos^5\theta$$
$$-\frac{8}{3}\cos^6\theta+\left(-\frac{\sqrt{3}}{6}\cos\theta+\frac{1}{3}\cos^2\theta+\frac{2\sqrt{3}}{3}\cos^3\theta-\frac{4}{3}\cos^4\theta\right)\sin\theta$$

$$N_9(\theta)=-\cos\theta+2\cos^2\theta+\frac{7}{3}\cos^3\theta-\frac{14}{3}\cos^4\theta-\frac{4}{3}\cos^5\theta+\frac{8}{3}\cos^6\theta$$
$$+\left(\frac{\sqrt{3}}{2}\cos\theta-\sqrt{3}\cos^2\theta-\frac{2\sqrt{3}}{3}\cos^3\theta+\frac{4\sqrt{3}}{3}\cos^4\theta\right)\sin\theta$$

$$N_{10}(\theta)=\frac{1}{2}-\frac{19}{6}\cos^2\theta+\frac{16}{3}\cos^4\theta-\frac{8}{3}\cos^6\theta+\left(-\frac{1}{2}+\frac{8}{3}\cos^2\theta-\frac{8}{3}\cos^4\theta\right)\sin\theta$$

$$N_{11}(\theta)=\cos\theta+2\cos^2\theta-\frac{7}{3}\cos^3\theta-\frac{14}{3}\cos^4\theta+\frac{4}{3}\cos^5\theta+\frac{8}{3}\cos^6\theta$$
$$+\left(-\frac{\sqrt{3}}{2}\cos\theta-\sqrt{3}\cos^2\theta+\frac{2\sqrt{3}}{3}\cos^3\theta+\frac{4\sqrt{3}}{3}\cos^4\theta\right)\sin\theta$$

$$N_{12}(\theta)=-\frac{\sqrt{3}}{3}\cos\theta-\frac{2}{3}\cos^2\theta+\frac{5\sqrt{3}}{3}\cos^3\theta+\frac{10}{3}\cos^4\theta-\frac{4\sqrt{3}}{3}\cos^5\theta$$
$$-\frac{8}{3}\cos^6\theta+\left(+\frac{\sqrt{3}}{6}\cos\theta+\frac{1}{3}\cos^2\theta-\frac{2\sqrt{3}}{3}\cos^3\theta-\frac{4}{3}\cos^4\theta\right)\sin\theta$$

16-node hole element:

$$N_1(\theta)=-\frac{1}{2}\cos\theta-\frac{1}{2}\cos^2\theta+5\cos^3\theta+5\cos^4\theta$$
$$-12\cos^5\theta-12\cos^6\theta+8\cos^7\theta+8\cos^8\theta$$

$$N_2(\theta)=\sqrt{1-\frac{\sqrt{2}}{2}}\cos\theta+\left(2-\sqrt{2}\right)\cos^2\theta-\sqrt{29-\frac{\sqrt{2}}{2}}\cos^3\theta-\left(10-3\sqrt{2}\right)$$
$$\cos^4\theta+\sqrt{100+34\sqrt{2}}\cos^5\theta+\left(16-2\sqrt{2}\right)\cos^6\theta-4\sqrt{2+\sqrt{2}}\cos^7\theta$$
$$-8\cos^8\theta+\left(\frac{\sqrt{2}-1}{2}\cos\theta+\sqrt{\frac{10-7\sqrt{2}}{2}}\cos^2\theta-\left(2\sqrt{2}-1\right)\cos^3\theta\right.$$
$$\left.-\sqrt{52-34\sqrt{2}}\cos^4\theta+2\sqrt{2}\cos^5\theta+4\sqrt{2-\sqrt{2}}\cos^6\theta\right)\sin\theta$$

$$N_3(\theta)=-\frac{\sqrt{2}}{2}\cos\theta-\cos^2\theta+\frac{9\sqrt{2}}{2}\cos^3\theta+9\cos^4\theta-8\sqrt{2}\cos^5\theta$$
$$-16\cos^6\theta+4\sqrt{2}\cos^7\theta+8\cos^8\theta+\left(-\frac{1}{2}\cos\theta-\frac{\sqrt{2}}{2}\cos^2\theta\right.$$
$$\left.+4\cos^3\theta+4\sqrt{2}\cos^4\theta-4\cos^5\theta-4\sqrt{2}\cos^6\theta\right)\sin\theta$$

$$N_4(\theta)=\sqrt{1+\frac{\sqrt{2}}{2}}\cos\theta+\left(2+\sqrt{2}\right)\cos^2\theta-\sqrt{29+\frac{\sqrt{2}}{2}}\cos^3\theta-\left(10+3\sqrt{2}\right)$$
$$\cos^4\theta+\sqrt{100-34\sqrt{2}}\cos^5\theta+\left(16+2\sqrt{2}\right)\cos^6\theta-4\sqrt{2-\sqrt{2}}\cos^7\theta$$
$$-8\cos^8\theta+\left(\frac{\sqrt{2}+1}{2}\cos\theta+\sqrt{\frac{10+7\sqrt{2}}{2}}\cos^2\theta-\left(2\sqrt{2}+1\right)\cos^3\theta\right.$$
$$\left.-\sqrt{52+34\sqrt{2}}\cos^4\theta+2\sqrt{2}\cos^5\theta+4\sqrt{2+\sqrt{2}}\cos^6\theta\right)\sin\theta$$

$$N_5(\theta)=\frac{1}{2}-\frac{11}{2}\cos^2\theta+17\cos^4\theta-20\cos^6\theta+8\cos^8\theta$$
$$+\left(\frac{1}{2}-5\cos^2\theta+12\cos^4\theta-8\cos^6\theta\right)\sin\theta$$

$$N_6(\theta)=-\sqrt{1-\frac{\sqrt{2}}{2}}\cos\theta+\left(2-\sqrt{2}\right)\cos^2\theta+\sqrt{29-\frac{\sqrt{2}}{2}}\cos^3\theta-\left(10-3\sqrt{2}\right)$$
$$\cos^4\theta-\sqrt{100+34\sqrt{2}}\cos^5\theta+\left(16-2\sqrt{2}\right)\cos^6\theta+4\sqrt{2+\sqrt{2}}\cos^7\theta$$
$$-8\cos^8\theta+\left(-\frac{\sqrt{2}-1}{2}\cos\theta+\sqrt{\frac{10-7\sqrt{2}}{2}}\cos^2\theta+\left(2\sqrt{2}-1\right)\cos^3\theta\right.$$
$$\left.-\sqrt{52-34\sqrt{2}}\cos^4\theta-2\sqrt{2}\cos^5\theta+4\sqrt{2-\sqrt{2}}\cos^6\theta\right)\sin\theta$$

$$N_7(\theta)=\frac{\sqrt{2}}{2}\cos\theta-\cos^2\theta-\frac{9\sqrt{2}}{2}\cos^3\theta+9\cos^4\theta+8\sqrt{2}\cos^5\theta$$
$$-16\cos^6\theta-4\sqrt{2}\cos^7\theta+8\cos^8\theta+\left(\frac{1}{2}\cos\theta-\frac{\sqrt{2}}{2}\cos^2\theta\right.$$
$$\left.-4\cos^3\theta+4\sqrt{2}\cos^4\theta+4\cos^5\theta-4\sqrt{2}\cos^6\theta\right)\sin\theta$$

$$N_8(\theta) = -\sqrt{1-\frac{\sqrt{2}}{2}}\cos\theta + \left(2-\sqrt{2}\right)\cos^2\theta + \sqrt{29-\frac{\sqrt{2}}{2}}\cos^3\theta - \left(10-3\sqrt{2}\right)$$
$$\cos^4\theta - \sqrt{100+34\sqrt{2}}\cos^5\theta + \left(16-2\sqrt{2}\right)\cos^6\theta + 4\sqrt{2+\sqrt{2}}\cos^7\theta$$
$$-8\cos^8\theta + \left(-\frac{\sqrt{2}-1}{2}\cos\theta + \sqrt{\frac{10-7\sqrt{2}}{2}}\cos^2\theta + \left(2\sqrt{2}-1\right)\cos^3\theta\right.$$
$$\left.-\sqrt{52-34\sqrt{2}}\cos^4\theta - 2\sqrt{2}\cos^5\theta + 4\sqrt{2-\sqrt{2}}\cos^6\theta\right)\sin\theta$$

$$N_9(\theta) = \frac{1}{2}\cos\theta - \frac{1}{2}\cos^2\theta - 5\cos^3\theta + 5\cos^4\theta$$
$$+12\cos^5\theta - 12\cos^6\theta - 8\cos^7\theta + 8\cos^8\theta$$

$$N_{10}(\theta) = -\sqrt{1-\frac{\sqrt{2}}{2}}\cos\theta + \left(2-\sqrt{2}\right)\cos^2\theta + \sqrt{29-\frac{\sqrt{2}}{2}}\cos^3\theta - \left(10-3\sqrt{2}\right)$$
$$\cos^4\theta - \sqrt{100+34\sqrt{2}}\cos^5\theta + \left(16-2\sqrt{2}\right)\cos^6\theta + 4\sqrt{2+\sqrt{2}}\cos^7\theta$$
$$-8\cos^8\theta + \left(\frac{\sqrt{2}-1}{2}\cos\theta - \sqrt{\frac{10-7\sqrt{2}}{2}}\cos^2\theta - \left(2\sqrt{2}-1\right)\cos^3\theta\right.$$
$$\left.+\sqrt{52-34\sqrt{2}}\cos^4\theta + 2\sqrt{2}\cos^5\theta - 4\sqrt{2-\sqrt{2}}\cos^6\theta\right)\sin\theta$$

$$N_{11}(\theta) = \frac{\sqrt{2}}{2}\cos\theta - \cos^2\theta - \frac{9\sqrt{2}}{2}\cos^3\theta + 9\cos^4\theta + 8\sqrt{2}\cos^5\theta$$
$$-16\cos^6\theta - 4\sqrt{2}\cos^7\theta + 8\cos^8\theta + \left(-\frac{1}{2}\cos\theta + \frac{\sqrt{2}}{2}\cos^2\theta\right.$$
$$\left.+4\cos^3\theta - 4\sqrt{2}\cos^4\theta - 4\cos^5\theta + 4\sqrt{2}\cos^6\theta\right)\sin\theta$$

$$N_{12}(\theta) = -\sqrt{1-\frac{\sqrt{2}}{2}}\cos\theta + \left(2-\sqrt{2}\right)\cos^2\theta + \sqrt{29-\frac{\sqrt{2}}{2}}\cos^3\theta - \left(10-3\sqrt{2}\right)$$
$$\cos^4\theta - \sqrt{100+34\sqrt{2}}\cos^5\theta + \left(16-2\sqrt{2}\right)\cos^6\theta + 4\sqrt{2+\sqrt{2}}\cos^7\theta$$
$$-8\cos^8\theta + \left(\frac{\sqrt{2}-1}{2}\cos\theta - \sqrt{\frac{10-7\sqrt{2}}{2}}\cos^2\theta - \left(2\sqrt{2}-1\right)\cos^3\theta\right.$$
$$\left.+\sqrt{52-34\sqrt{2}}\cos^4\theta + 2\sqrt{2}\cos^5\theta - 4\sqrt{2-\sqrt{2}}\cos^6\theta\right)\sin\theta$$

$$N_{13}(\theta) = \frac{1}{2} - \frac{11}{2}\cos^2\theta + 17\cos^4\theta - 20\cos^6\theta + 8\cos^8\theta +$$
$$\left(-\frac{1}{2} + 5\cos^2\theta - 12\cos^4\theta + 8\cos^6\theta\right)\sin\theta$$

$$N_{14}(\theta) = \sqrt{1+\frac{\sqrt{2}}{2}}\cos\theta + \left(2+\sqrt{2}\right)\cos^2\theta - \sqrt{29+\frac{\sqrt{2}}{2}}\cos^3\theta - \left(10+3\sqrt{2}\right)$$
$$\cos^4\theta + \sqrt{100-34\sqrt{2}}\cos^5\theta + \left(16+2\sqrt{2}\right)\cos^6\theta - 4\sqrt{2-\sqrt{2}}\cos^7\theta$$
$$-8\cos^8\theta + \left(-\frac{\sqrt{2}+1}{2}\cos\theta - \sqrt{\frac{10+7\sqrt{2}}{2}}\cos^2\theta + \left(2\sqrt{2}+1\right)\cos^3\theta\right.$$
$$\left.+\sqrt{52+34\sqrt{2}}\cos^4\theta - 2\sqrt{2}\cos^5\theta - 4\sqrt{2+\sqrt{2}}\cos^6\theta\right)\sin\theta$$

$$N_{15}(\theta) = -\frac{\sqrt{2}}{2}\cos\theta - \cos^2\theta + \frac{9\sqrt{2}}{2}\cos^3\theta + 9\cos^4\theta - 8\sqrt{2}\cos^5\theta$$
$$-16\cos^6\theta + 4\sqrt{2}\cos^7\theta + 8\cos^8\theta + \left(\frac{1}{2}\cos\theta + \frac{\sqrt{2}}{2}\cos^2\theta\right.$$
$$\left.-4\cos^3\theta - 4\sqrt{2}\cos^4\theta + 4\cos^5\theta + 4\sqrt{2}\cos^6\theta\right)\sin\theta$$

$$N_{16}(\theta) = \sqrt{1 - \frac{\sqrt{2}}{2}}\cos\theta + \left(2 - \sqrt{2}\right)\cos^2\theta - \sqrt{29 - \frac{\sqrt{2}}{2}}\cos^3\theta - \left(10 - 3\sqrt{2}\right)$$
$$\cos^4\theta + \sqrt{100 + 34\sqrt{2}}\cos^5\theta + \left(16 - 2\sqrt{2}\right)\cos^6\theta - 4\sqrt{2 + \sqrt{2}}\cos^7\theta$$
$$-8\cos^8\theta + \left(-\frac{\sqrt{2} - 1}{2}\cos\theta - \sqrt{\frac{10 - 7\sqrt{2}}{2}}\cos^2\theta + \left(2\sqrt{2} - 1\right)\cos^3\theta\right.$$
$$\left.+\sqrt{52 - 34\sqrt{2}}\cos^4\theta - 2\sqrt{2}\cos^5\theta - 4\sqrt{2 - \sqrt{2}}\cos^6\theta\right)\sin\theta$$

References

[1] Zienkiewicz OC, Taylor RL. The finite element method. sixth ed. London: Elsevier; 2005.
[2] Hughes TJR. The finite element method: linear static and dynamic finite element analysis. Englewood Cliffs, N.J.: Prentice-Hall; 1987.
[3] Liu GR, Quek SS. The finite element method: a practical course. Second. Oxford, UK: Butterworth-Heinemann Elsevier; 2003.
[4] Brebbia CA, Dominguez J. Boundary elements: an introductory course. Southampton: Computational Mechanics Publications; 1992.
[5] Gao XW, David TG. Boundary element programming in mechanics. Cambridge, UK: Cambridge University Press; 2002.
[6] Liu Y. Fast multipole boundary element method: theory and applications in engineering. Cambridge: Cambridge University Press; 2009.
[7] Henry DP, Banerjee PK. Elastic stress analysis of three-dimensional solids with small holes by BEM. Int J Numer Methods Eng 1991;31:369–84. https://doi.org/10.1002/nme.1620310210.
[8] Banerjee PK, Henry DP. Elastic analysis of three-dimensional solids with fiber inclusions by BEM. Int J Solids Struct 1992;29:2423–40. https://doi.org/10.1016/0020-7683(92)90001-A.
[9] Henry DP, Ma F, Chatterjee J, Banerjee PK. Steady state thermoelastic analysis of 3D solids with fiber inclusions by boundary element method. Comput Methods Appl Mech Eng 2007;197:294–307. https://doi.org/10.1016/j.cma.2007.08.001.
[10] Chatterjee J, Henry DP, Ma F, Banerjee PK. An efficient BEM formulation for three-dimensional steady-state heat conduction analysis of composites. Int J Heat Mass Transf 2008;51:1439–52. https://doi.org/10.1016/j.ijheatmasstransfer.2007.09.004.
[11] Buroni FC, Marczak RJ. A family of hole boundary elements for modeling materials with cylindrical voids. Eng Anal Bound Elem 2008;32:578–90. https://doi.org/10.1016/j.enganabound.2007.11.003.
[12] Buroni FC, Marczak RJ. Effective properties of materials with random micro-cavities using special boundary elements. J Mater Sci 2008;43:3510–21. https://doi.org/10.1007/s10853-008-2479-3.
[13] Qin X, Zhang J, Liu L, Li G. Steady-state heat conduction analysis of solids with small open-ended tubular holes by BFM. Int J Heat Mass Transf 2012;55:6846–53. https://doi.org/10.1016/j.ijheatmasstransfer.2012.06.091.
[14] Huang C, Zhang J, Qin X, Lu C, Sheng X, Li G. Stress analysis of solids with open-ended tubular holes by BFM. Eng Anal Bound Elem 2012;36:1908–16. https://doi.org/10.1016/j.enganabound.2012.07.009.
[15] Wang X, Lu C, Zhou F, Zheng X, Zhang J. Acoustic problems analysis of 3D solid with small holes by fast multipole boundary face method. Eng Anal Bound Elem 2013;37:1703–11. https://doi.org/10.1016/j.enganabound.2013.09.013.
[16] Feng J, Yao Z, Liu Y, Zou Y, Zheng X. Some spherical boundary elements and a discretization error indicator for acoustic problems with spherical surfaces. Eng Anal Bound Elem 2015;56:176–89. https://doi.org/10.1016/j.enganabound.2015.01.018.
[17] Gao XW, Yuan ZC, Peng HF, Cui M, Yang K. Isoparametric closure elements in boundary element method. Comput Struct 2016;168:1–15. https://doi.org/10.1016/j.compstruc.2016.02.002.
[18] Gao XW, Zheng YT, Peng HF, Cui M, Zhang ZY. Trans-accuracy elements and their application in BEM analysis of structurally multi-scale problems. Eng Anal Bound Elem 2018;97:82–93. https://doi.org/10.1016/j.enganabound.2018.09.011.
[19] Gao XW, Zeng WH, Cui M. Isoparametric tube elements and their application in heat conduction BEM analysis. Chinese J Comput Mech 2016;33:328–34. https://doi.org/10.7511/jslx201603008.
[20] Ma H, Tian Y, He D. High order isoparametric elements in boundary element method—Smooth elliptical element. Eng Anal Bound Elem 2019;101:37–47. https://doi.org/10.1016/j.enganabound.2018.12.009.
[21] Ma H, He D, Tian Y. High order isoparametric elements in boundary element method—Smooth spheroidal element. Eng Anal Bound Elem 2019;104:34–45. https://doi.org/10.1016/j.enganabound.2019.03.019.
[22] Brebbia CA, Telles JCF, Wrobel LC. Boundary element techniques. 1st ed. Berlin, Heidelberg: Springer; 1984. https://doi.org/10.1007/978-3-642-48860-3.
[23] Gao XW, Yang K, Wang J. An adaptive element subdivision technique for evaluation of various 2D singular boundary integrals. Eng Anal Bound Elem 2008;32:692–6. https://doi.org/10.1016/j.enganabound.2007.12.004.